

# 1 **A dynamic parameterization of sulfuric acid-dimethylamine** 2 **nucleation and its application in three-dimensional modeling**

3 Yuyang Li<sup>1, #</sup>, Jiewen Shen<sup>1, 2, #</sup>, Bin Zhao<sup>1, 2, \*</sup>, Runlong Cai<sup>3</sup>, Shuxiao Wang<sup>1, 2</sup>, Yang Gao<sup>4</sup>, Manish Shrivastava<sup>5</sup>, Da Gao<sup>1, 2</sup>,  
4 Jun Zheng<sup>6</sup>, Markku Kulmala<sup>2, 7, 8</sup>, Jingkun Jiang<sup>1, \*</sup>

5  
6 <sup>1</sup>State Key Joint Laboratory of Environment Simulation and Pollution Control, School of Environment, Tsinghua University,  
7 100084 Beijing, China

8 <sup>2</sup>State Environmental Protection Key Laboratory of Sources and Control of Air Pollution Complex, Beijing, 100084, China

9 <sup>3</sup>Institute for Atmospheric and Earth System Research/Physics, Faculty of Science, University of Helsinki, 00014 Helsinki,  
10 Finland

11 <sup>4</sup>Key Laboratory of Marine Environment and Ecology, Ministry of Education, Ocean University of China, Qingdao 266100,  
12 China

13 <sup>5</sup>Pacific Northwest National Laboratory, Richland, Washington, USA

14 <sup>6</sup>School of Environmental Science and Engineering, Nanjing University of Information Science & Technology, Nanjing  
15 210044, China

16 <sup>7</sup>Aerosol and Haze Laboratory, Beijing Advanced Innovation Center for Soft Matter Science and Engineering, Beijing  
17 University of Chemical Technology, 100029 Beijing, China

18 <sup>8</sup>Joint International Research Laboratory of Atmospheric and Earth System Sciences, School of Atmospheric Sciences,  
19 Nanjing University, Nanjing, China

20 # These authors contributed equally

21 \* *Correspondence to:* Bin Zhao (bzhaob@mail.tsinghua.edu.cn) and Jingkun Jiang (jiangjk@tsinghua.edu.cn)

22 **Abstract.** Sulfuric acid (SA) is a governing gaseous precursor for atmospheric new particle formation (NPF), a major source  
23 of global ultrafine particles, in environments studied around the world. In polluted urban atmospheres with high condensation  
24 sink (CS), the formation of stable SA-amine clusters, such as SA-DMA clusters, usually initializes intense NPF events.  
25 Coagulation scavenging and cluster evaporation are dominant sink processes of SA-amine clusters in urban atmospheres, yet  
26 these loss processes are not quantitatively included in the present parameterizations of SA-amine nucleation. We herein report  
27 a parameterization of SA-DMA nucleation based on cluster dynamic simulations and quantum chemistry calculations, with  
28 certain simplifications to greatly reduce the computational costs. Compared with previous SA-DMA nucleation  
29 parameterizations, this new parameterization was able to reproduce the dependences of particle formation rates on temperature  
30 and CS. We then incorporated it in a three-dimensional chemical transport model to simulate the evolution of particle number  
31 size distributions. Simulation results showed good consistency with the observations in the occurrence of NPF events and  
32 particle number size distributions in wintertime Beijing, and represented a significant improvement compared to that using  
33 parameterization without coagulation scavenging. Quantitative analysis shows that SA-DMA nucleation contributes  
34 significantly to nucleation rates and aerosol population during the 3-D simulations in Beijing (>99% and >60%, respectively).  
35 These results broaden the understanding of NPF in urban atmospheres and stress the necessity of including the effects of  
36 coagulation scavenging and cluster stability in simulating SA-DMA nucleation in three-dimensional simulations. Representing  
37 these processes is thus likely to improve model performance in particle source apportionment and quantification of aerosol  
38 effects on air quality, human health, and climate.

## 39 1 Introduction

40 New particle formation (NPF) is the major source of atmospheric particles in terms of their number concentration, which  
41 regulates the Earth's radiative balance and affects the climate (Kulmala et al., 2004; Gordon et al., 2017; Merikanto et al.,  
42 2009). The transformation from gaseous precursors to stable clusters and particles via nucleation is the initial step of NPF, and  
43 new particle formation rate ( $J$ ) is an essential parameter to characterize NPF intensity (Kulmala, 2003). Although nucleation  
44 processes would be suppressed by coagulation scavenging in urban atmospheres with high condensation sink (CS) (Cai and  
45 Jiang, 2017; Cai et al., 2017b), intense NPF events have been frequently observed (Wu et al., 2007; Xiao et al., 2015; Deng et  
46 al., 2020). Recently increasing evidence has been provided that those intense events are driven by the formation of stable SA-  
47 amine clusters (Cai et al., 2022; Jen et al., 2014b; Yin et al., 2021) with a speed close to the collision limit for SA molecules,  
48 thus deriving high nucleation rates in urban atmospheres (Cai et al., 2021d; Yao et al., 2018; Chen et al., 2012). Furthermore,  
49 other molecules, such as  $\text{HNO}_3$  and  $\text{NH}_3$ , could enhance the SA-DMA nucleation under certain conditions (Liu et al., 2021;  
50 Glasoe et al., 2015; Wang et al., 2021). Although a few previous 3-D simulation studies have simulated NPF events in polluted  
51 urban atmospheres such as Beijing, they didn't take the SA-amine nucleation into account (Chen et al., 2019; Chen et al.,  
52 2021b). Thus, integrating SA-amine nucleation into three-dimensional (3-D) models is essential in extending the understanding  
53 of NPF in polluted urban areas and quantifying its underlying impacts on the environment and climate. This requires a  
54 quantitative representation of particle formation rates through SA-amine nucleation for 3-D models.

55 Semi-empirical power-law functions are widely used in SA-relevant nucleation rate studies to fit the experimental data, which  
56 has been shown to reproduce the measured  $J$  in certain ambient observations or experimental conditions (Riccobono et al.,  
57 2014; Dunne et al., 2016; Bergman et al., 2015; Hanson et al., 2017; Semeniuk and Dastoor, 2018; Kurten et al., 2014; Kurten  
58 et al., 2018). For SA-amine nucleation, Bergman et al. (2015) and Dunne et al. (2016) have presented semi-empirical  
59 parameterizations of good consistencies with chamber and flow-tube experimental results (Almeida et al., 2013; Jen et al.,  
60 2014b; Glasoe et al., 2015). In real urban atmospheres, recent advances have shown that coagulation scavenging would greatly  
61 suppress concentrations of molecular clusters, and thus the nucleation rates (Cai and Jiang, 2017; Cai et al., 2021c; Cai et al.,  
62 2021d; Marten et al., 2022). It has also been addressed that the formation of the smallest SA-amine clusters, which is largely  
63 dependent on cluster stability, is the limiting step for SA-amine nucleation rates (Cai et al., 2022). However, the effects of  
64 coagulation scavenging and cluster stability vary with the environmental factors, e.g., CS and temperature, while these effects  
65 have not been well represented in semi-empirical power-law functions derived from certain experimental systems or ambient  
66 environments. Cluster kinetic simulations coupled with quantum chemistry calculations (Mcgrath et al., 2012), which take into  
67 account the effects of both coagulation scavenging and cluster stability, have been widely applied in zero-dimensional or one-  
68 dimensional simulations of SA- $\text{NH}_3$  or SA-amine nucleation (Yang et al., 2021; Lu et al., 2020; Yao et al., 2018; Yu, 2006;  
69 Yu and Turco, 2001). Specifically, both cluster kinetic simulations and observations reveal that dimethylamine (DMA) is  
70 plausibly most efficient in stabilizing SA clusters and is regarded as the key amine species deriving high particle formation  
71 rates in urban atmospheres (Jen et al., 2014b; Cai et al., 2022; Yao et al., 2018; Chen et al., 2012). However, no method with  
72 good representations of coagulation scavenging and cluster stabilities has been reported to explicitly simulate the SA-DMA  
73 nucleation rates in 3-D chemical transport models.

74 A challenge in setting up a parameterization based on cluster kinetic simulations for 3-D chemical transport models is to reduce  
75 computational costs and yield explicit expressions. A plausible method to reduce computational costs is to omit the unstable  
76 clusters with high evaporation rates from the nucleation pathway. Accordingly, different nucleation schemes were presented  
77 to represent the dominant source or sink processes of SA-DMA clusters in specific chamber experiments or ambient  
78 environments (Lu et al., 2020; Cai et al., 2021d). For polluted urban atmospheres, a kinetic model with a key pathway of  
79 particle formation in SA-DMA nucleation was constructed, yielding good predictions of measured SA cluster concentrations  
80 and 1.4 nm particle formation rates ( $J_{1.4}$ ) in urban Beijing (Cai et al., 2021d). Application of pseudo-steady-state assumptions

81 is also an alternative method for reducing computational costs and yielding explicit expressions. The NPF occurrence indicator  
82 ( $I$ ) based on the kinetic model with pseudo-steady-state assumptions has shown good consistency in qualitatively estimating  
83 the NPF events in urban Beijing and Shanghai (Cai et al., 2021c). These results indicate the potential of deriving an explicit  
84 parameterization of particle formation rates by applying pseudo-steady-state assumptions to the kinetic model, although further  
85 quantitative analysis is still required to validate this parameterization.

86 In this study, we set up an SA-DMA nucleation parameterization, which is designed for application in 3-D chemical transport  
87 models. The parameterization is based on the pseudo-steady-state particle formation rate in the kinetic model, with a full  
88 representative of the effects of coagulation scavenging and cluster stability (Cai et al., 2021d). Generally, only four variables  
89 (temperature  $T$ , CS, gaseous DMA concentrations  $[B]$ , and concentrations of SA molecules or clusters containing one SA  
90 molecule  $[SA_{tot}]$ ) are used in the parameterization, with computational costs greatly reduced. We then implement the  
91 parameterization in a 3-D chemical transport model and combine it with an integrated source-sink representation of DMA to  
92 simulate the evolution of the particle number size distributions (PNSDs) in wintertime Beijing. The precursor concentrations,  
93 PNSDs, NPF occurrence and  $J_{1.4}$  show relatively good consistencies between simulations and observations. The simulations  
94 show that the SA-DMA nucleation contributes >99% of the  $J_{1.4}$  and >60% of the total particle number concentration in  
95 wintertime Beijing, respectively. With this parameterization, 3-D chemical transport models could significantly improve the  
96 simulation of NPF, especially in urban environments, and thus the effects of NPF on particulate matter pollution or climate.

## 97 **2 Methods**

### 98 **2.1 Derivation of Parameterized Formation Rate in SA-DMA Nucleation**

99 Limited by computational quantum chemistry calculation results, SA-DMA nucleation is commonly simulated in the range of  
100 clusters containing not more than 4 SA or 4 DMA molecules (Olenius et al., 2013; Ortega et al., 2012). As unstable clusters  
101 would evaporate with higher rates, the formation of larger clusters potentially follows the pathways of the most stable clusters.  
102 In addition, as the SA-DMA clusters are increasingly stable along the main pathway of cluster formation, the clusters not  
103 smaller than  $A_4B_4$  (hereafter  $A_mB_n$  refers to clusters containing  $m$  SA and  $n$  DMA molecules) is assumed to not evaporate back  
104 in these simulations. Although there are uncertainties in the pathways presented based on different quantum chemistry methods,  
105 it is well accepted that the  $A_mB_m$  ( $m=1$  to 4) and  $A_2B_1$  clusters are relatively stable in the SA-DMA nucleation scheme (Olenius  
106 et al., 2017; Olenius et al., 2013; Ortega et al., 2012; Myllys et al., 2019).

107 Based on previous studies under atmospheric conditions, the variation of precursor concentrations, temperature, and CS do  
108 not result in large deviations in the main pathway. Previous simulations under different  $[SA]$ ,  $[DMA]$ , and temperature have  
109 shown that the main pathway was similar under the different conditions studied (Olenius et al., 2013). The effect of CS on  
110 nucleation pathway is dependent on the relative relationship between the coagulation sink and the evaporation rate of a certain  
111 cluster. For most clusters out of the specified pathway, the evaporation rates are much higher than the typical CS range in  
112 urban atmospheres (Ortega et al., 2012), therefore such clusters would not dominate the nucleation pathway no matter how  
113 low or high the CS is. Thus in this study, the variation of the dominant pathway under different conditions was ignored.

114 Accordingly, the parameterization in this study is derived from the nucleation pathway including  $A$ ,  $B$  and other 5 SA-DMA  
115 clusters ( $A_mB_m$  ( $m=1$  to 4) and  $A_2B_1$ ), consistent with a previous study (Cai et al., 2021d). The clusters except  $A_4B_4$  are assumed  
116 to be in pseudo-steady states, i.e. the sink due to evaporation, coagulation scavenging, and cluster collision is equal to the  
117 source due to the collisions of molecules or smaller clusters. As the  $A_4B_4$  clusters are estimated to be with an electrical mobility  
118 diameter of approximately 1.4 nm, the pseudo-steady-state formation rate of  $A_4B_4$  was applied in the parameterization of  $J_{1.4}$   
119 in this study. Although some studies have revealed that SA-DMA nucleation could also be enhanced by adding other molecules

120 in certain conditions, quantitative analysis of these effects in relevant atmospheric conditions is still lacking, thus in this study,  
 121 we set up this parameterization only based on SA-DMA binary nucleation.

### 122 2.1.1 Derivation of Collision Coefficients, Coagulation Sink, and Evaporation Rates

123 In the nucleation pathway discussed above,  $A$ ,  $B$ , and 5 SA-DMA clusters are included. The collision coefficients between  
 124 them ( $\beta_{i-j}$ ) and the evaporation rate of  $A_1B_1$  clusters ( $\gamma$ ) vary with  $T$  during the simulation. The coagulation sinks (CoagS <sub>$i$</sub> ) due  
 125 to the coagulation scavenging of background aerosols are dependent on CS. The work discussed in this section is focused on  
 126 simplification of the derivation of these parameters to be updated in each simulation time interval to reduce the computational  
 127 costs.

128 As the involved clusters and molecules are in the free molecular regime (Knudsen number  $> 10$ ),  $\beta_{i-j}$  in SA-DMA nucleation  
 129 processes can be calculated based on kinetic gas theory (Seinfeld and Pandis, 1998; Olenius et al., 2013; Ortega et al., 2012):

$$130 \beta_{i-j} = \left(\frac{3}{4\pi}\right)^{1/6} \left(\frac{1}{m_i} + \frac{1}{m_j}\right)^{1/2} (V_i^{1/3} + V_j^{1/3})^2 (6k_b T)^{1/2} E_{ij}, \quad (1)$$

131 where  $m$  (kg) and  $V$  (m<sup>3</sup>) represent the molecular mass and molecular volume, respectively. The density of precursor molecules  
 132  $A$  and  $B$  was assumed to be 1830 and 680 kg m<sup>-3</sup>, respectively.  $T$  (K) represents the temperature.  $k_b$  (J K<sup>-1</sup>) is the Boltzmann  
 133 constant. Subscripts  $i$  and  $j$  refer to the index of the clusters or molecules (1 to 7 refer to  $A$ ,  $B$ ,  $A_1B_1$ ,  $A_2B_1$ ,  $A_2B_2$ ,  $A_3B_3$ , and  $A_4B_4$ ,  
 134 respectively, which are involved in the kinetic model).  $E_{ij}$  is a dimensionless enhancement factor of the collision rates from  
 135 Van de Waals forces between  $i$  and  $j$ . In this study,  $E_{ij}$  is assumed to be 2.3 (Chan and Mozurkewich, 2001; Sceats, 1989),  
 136 within the range of 2.3 to 2.7 predicted by Brownian coagulation models, and consistent with the value used in other cluster  
 137 dynamics studies (Kurten et al., 2014; Lehtipalo et al., 2016; Stolzenburg et al., 2020).

138 Noting that  $m_i$  and  $V_i$  are almost independent of the atmospheric conditions and  $E_{ij}$  is assumed to be constant, we can normalize  
 139 different values of  $\beta_{i-j}$  into  $\beta$ , and the normalizing factor is shown in a look-up table (Table S1 in the supporting information  
 140 (SI)) as  $G(i,j)$ :

$$141 \beta_{i-j} = \beta G(i, j), \quad (2)$$

142 where  $\beta$  represents the collision coefficients between two  $A_1B_1$  clusters ( $\beta_{3,3}$ ), and could be calculated as:

$$143 \beta = \beta_0 \left(\frac{T}{T_0}\right)^{0.5}, \quad (3)$$

144 where  $\beta_0$  is the value of  $\beta$  at the standard temperature  $T_0=298.15$  K, constant as  $1.126 \times 10^{-15}$  m<sup>3</sup> s<sup>-1</sup>.

145 Similarly, CoagS <sub>$i$</sub>  could also be normalized to CS using fixed ratios. The size dependent coagulation sink (CoagS) is calculated  
 146 with a power-law exponent of -1.7, within the typical range of atmospheric aerosols (Lehtinen et al., 2007):

$$147 CoagS_i = CS \left(\frac{V_i}{V_1}\right)^{\frac{1.7}{3}} = H(i)CS, \quad (4)$$

148 where the dimensionless factors  $H(i)$  are also recorded in Table S1 in the SI.

149 The evaporation rates of  $A_1B_1$  could be derived based on collision-evaporation equilibrium (Ortega et al., 2012), closely  
 150 relevant to the free energy barrier to form  $A_1B_1$  clusters (Olenius et al., 2013; Ortega et al., 2012):

$$151 \gamma = \beta_{1-2} c_{\text{ref}} \exp\left(\frac{\Delta G}{k_B T}\right), \quad (5)$$

152 where  $c_{\text{ref}}$  is the number concentrations under standard conditions ( $2.46 \times 10^{25}$  m<sup>-3</sup>).  $\Delta G$  is the formation free energies of  $A_1B_1$ .  
 153 Thus if we take  $T_0 = 298.15$  as a reference,  $\gamma$  could also be calculated as:

$$154 \gamma = \gamma_0 \left(\frac{T}{T_0}\right)^{0.5} \exp\left(\frac{\Delta H}{k_B} \left(\frac{1}{T} - \frac{1}{T_0}\right)\right), \quad (6)$$

$$\gamma_0 = \gamma'_0 \exp\left(\frac{\Delta G - \Delta G_0}{k_B T_0}\right), \quad (7)$$

where  $\gamma'_0$ , with the value of  $3.33 \text{ s}^{-1}$ , is the evaporation rates of  $A_1B_1$  at  $T_0$  with  $\Delta G = \Delta G_0 = -13.54 \text{ kcal mol}^{-1}$ .  $\Delta H$  is the formation enthalpies of  $A_1B_1$ . In previous studies, several sets of  $\Delta H$  and  $\Delta G$  at specific temperatures were reported based on different quantum chemistry models (Myllys et al., 2019; Ortega et al., 2012; Ge et al., 2020a). Here we use  $\Delta H = -24.82 \text{ kcal mol}^{-1}$  and  $\Delta G = -13.54 \text{ kcal mol}^{-1}$  according to the results in Myllys et al. (2019). If the values of  $\Delta G$  need to be updated in future application of this parameterization, the values of  $\gamma_0$  should be updated as well based on Eq. 7. The sensitivity analysis of different values of  $\Delta H$  and  $\Delta G$  are discussed in the Results section.

Generally, with  $G(i,j)$  and  $H(i)$  fixed into the parameterization formula,  $\beta_{i,j}$  and  $\text{CoagS}_i$  could be normalized to  $\beta$  and CS. Additionally, the values of  $\gamma$  and  $\beta$  could be real-time updated at any simulation timestep based on Eqs. 3 and 6.

### 2.1.2 Formula of the SA-DMA Nucleation Parameterization

Applying the pseudo-steady-state assumptions to the key pathway discussed above (Eqs. S1 to S9) and achieving real-time  $\gamma$  ( $\text{s}^{-1}$ ) and  $\beta$  ( $\text{m}^3 \text{ s}^{-1}$ ) (Eqs. 3 and 6), we could derive an explicit formula of the parameterized  $J_{1,4}$  in this study (Eq. 8).

$$J_{1,4} = \frac{\beta \theta [A_1B_1]^4}{2([A_1B_1] + 0.39 \frac{\text{CS}}{\beta})} \left( \frac{0.23 \theta}{[A_1B_1] + 0.39 \frac{\text{CS}}{\beta}} + \frac{1.00}{[A_1B_1] + 0.31 \frac{\text{CS}}{\beta}} \right), \quad (8)$$

The above intermediate parameters are calculated as below:

$$[A_1B_1] = \frac{0.96[\mathbf{B}][\mathbf{SA}_{\text{tot}}]}{0.96[\mathbf{B}] + \frac{\gamma}{\beta} + 0.86[\mathbf{SA}_{\text{tot}}] + 0.63 \frac{\text{CS}}{\beta}}, \quad (9)$$

$$\theta = 1 + \frac{2[\mathbf{B}]}{1.16[\mathbf{B}] + 0.46 \frac{\text{CS}}{\beta}} \frac{[\mathbf{SA}_{\text{tot}}] - [A_1B_1]}{[A_1B_1]}, \quad (10)$$

$$\theta' = \frac{\theta(2.22[A_1B_1] + 0.86 \frac{\text{CS}}{\beta})}{\sqrt{(1.11[A_1B_1] + 0.43 \frac{\text{CS}}{\beta})^2 + 1.12\theta[A_1B_1]^2 + 1.11[A_1B_1] + 0.43 \frac{\text{CS}}{\beta}}}, \quad (11)$$

In Eqs. 8 to 11, the four input variables ( $T$  (K),  $\text{CS}$  ( $\text{s}^{-1}$ ),  $[\mathbf{B}]$  ( $\text{m}^{-3}$ ),  $[\mathbf{SA}_{\text{tot}}]$  ( $\text{m}^{-3}$ )) are shown in bold. Generally, only these four variable parameters are needed for the 3-D chemical transport models. Additionally, compared with directly coupling cluster dynamic simulations into 3-D chemical transport models, the parameterization of pseudo-steady-state  $J_{1,4}$  requires much less computational time.

## 2.2 Incorporating the Parameterization into Updated WRF-Chem/R2D-VBS Model

The updated parameterization of SA-DMA nucleation was incorporated in the WRF-Chem (Weather Research and Forecasting model with Chemistry). Before adding the SA-DMA nucleation, we already incorporated seven other NPF mechanisms in the model (Zhao et al., 2020): four inorganic pathways, including binary neutral/ion-induced SA- $\text{H}_2\text{O}$  nucleation and ternary neutral/ion-induced  $\text{NH}_3$ -SA- $\text{H}_2\text{O}$  nucleation; and three organic pathways, including pure-organic neutral/ion-induced organic nucleation and ternary nucleation involving organics and SA. The organic containing nucleation pathways are driven by ultra- and extremely low volatility organic compounds (ULVOC and ELVOC) with  $\text{O:C} > 0.4$ , converted from monoterpene autoxidation. The chemical transformation and volatility distribution of monoterpene is represented in the model by R2D-VBS (Radical Two-Dimensional Volatility Basis Set framework) with constrained parameters against experiments. More details of the R2D-VBS are given in our previous study (Zhao et al., 2020). The newly formed nano-sized particles and their initial size evolution are accounted in the MOSAIC module by 20 size bins covering 1 nm to 10  $\mu\text{m}$ . It is worth mentioning that the newly formed particles from SA-DMA nucleation are lumped into a lower aerosol size bin in the model than that of other seven pathways. This should be attributed to that our SA-DMA nucleation parameterization are formulated at a 1.4 nm-sized particle formation rate while the remaining ones are fitted based on measured particle formation rates from CLOUD Chamber at a

190 mobility diameter of 1.7 nm. Given that condensation of gaseous SA and DMA on pre-existing aerosols and nucleation occur  
191 simultaneously in the real atmosphere, in the model, we then use a time-integrated-averaged concentration of precursors over  
192 each time step to drive SA-DMA nucleation. The condensation sink for SA and DMA is calculated according to simulated  
193 real-time PNSDs. In addition, the consumption of both SA and DMA concentration during nucleation is also accounted in the  
194 model, in order to represent a comprehensive sources-sink simulation scheme of two precursors in combination with other  
195 settings.

### 196 **2.2.1 Sources and Sinks of Dimethylamine in the Updated WRF-Chem/R2D-VBS Model**

197 A regional or global bottom-up emission inventory of DMA is currently lacking, mostly due to scarce direct measurements  
198 (Yang et al., 2022; Zhu et al., 2022). In previous 3D model studies, amine/NH<sub>3</sub> emission ratios have often been used to estimate  
199 amine emissions due to the close correlation between NH<sub>3</sub> and DMA emissions. However, a fixed amine/NH<sub>3</sub> ratio is likely  
200 to overestimate the concentrations of amines in rural areas while underestimating those in urban areas, where high  
201 concentrations of amines have been reported (Yao et al., 2018; Bergman et al., 2015). Here, a set of source-dependent  
202 DMA/NH<sub>3</sub> emission ratio was used to develop the emission inventory of DMA based on (Mao et al., 2018). The ratios for  
203 different emission sectors were determined by a source apportionment analysis, based on a simultaneous observation of NH<sub>3</sub>,  
204 C1-C3 amines, NO<sub>x</sub>, and SO<sub>2</sub> and also meteorological factors at a suburban site in Nanjing (Zheng et al., 2015a). We applied  
205 the source-dependent emission ratios (0.0070, 0.0018, 0.0015, 0.0100, and 0.0009 for chemical–industrial, other industrial,  
206 agricultural, residential, and transportation source types, respectively) to NH<sub>3</sub> emissions in the ABaCAS-EI 2017 (Emission  
207 Inventory of Air Benefit and Cost and Attainment Assessment System) for China mainland and the IIASA 2015 emission  
208 inventory for other areas to build continental DMA emission inventory (Zheng et al., 2019; Li et al., 2017). In addition, DMA  
209 emission for maritime area was developed employing a DMA/NH<sub>3</sub> ratio derived from recent campaigns in offshore areas of  
210 China (see details in SI) (Chen et al., 2021a).

211 DMA can be removed from the atmosphere through three main pathways: gas-phase chemical reaction, aerosol uptake, and  
212 wet deposition, which are all explicitly considered in our model. For the gas-phase chemical reactions, only oxidation of DMA  
213 by •OH is included. Reactions with other oxidants (O<sub>3</sub> and NO<sub>3</sub>) are much slower and therefore have negligible effects on  
214 DMA concentrations (Ge et al., 2011). The mechanism of DMA concentration depletion by aerosol uptake is still poorly  
215 understood, and the key parameter, uptake coefficient  $\gamma_u$ , varies in a wide range depending on many factors such as aerosol  
216 composition and relative humidity. In this study, we assumed  $\gamma_u = 0.001$ , approximately a median value among those reported  
217 by recent laboratory measurements (Qiu et al., 2011; Wang et al., 2010). Regarding DMA depletion by wet deposition, the  
218 treatment is similar to that of NH<sub>3</sub> based on Henry's Law. The key parameters for above sink processes are summarized in  
219 Table S2 in the SI.

### 220 **2.2.2 Configuration of the Updated WRF-Chem/R2D-VBS Model.**

221 The WRF-Chem model configured with the SA-DMA nucleation is applied to a domain covering eastern Asia with a horizontal  
222 resolution of 27 km, where Beijing is located close to the center. The simulations are performed for two winter months  
223 separately (December 2018 and January 2019) with 5 days spin-up run for each month. The ABaCAS-EI 2017 and IIASA  
224 2015 emission inventory were used for China mainland and other areas, respectively. The biogenic emission is calculated by  
225 the Model of Emissions of Gases and Aerosols from Nature (MEGAN) v2.04 (Guenther et al., 2006). Except for the  
226 monoterpene-related gas and aerosol chemistry that is traced by R2D-VBS, the remaining gas- and aerosol chemical processes  
227 are simulated by the SAPRC99 gas chemistry scheme coupled with the MOSAIC (Model for Simulating Aerosol Interaction  
228 and Chemistry) aerosol module and a one-dimensional VBS set for SOA modeling (Zaveri et al., 2014; Shrivastava et al.,  
229 2019; Shrivastava et al., 2011).

230 Four scenario simulations with different configurations of the NPF mechanisms were conducted in this study to examine how  
231 the SA-DMA nucleation affects the simulations of aerosol size distribution: 1) 8 NPF mechanisms with the SA-DMA  
232 nucleation rate at 1.4 nm (abbr. DMA1.4\_Mech8); 2) 8 NPF mechanisms with the SA-DMA nucleation rate at 1.7 nm  
233 converted using modified Kerminen-Kulmala equation (Lehtinen et al., 2007) (DMA1.7\_Mech8); 3) 7 NPF mechanisms  
234 without the SA-DMA nucleation (NoDMA\_Mech7); and 4) No NPF mechanism (NoDMA\_Mech0). Among them, scenario 1  
235 is our “best-case” with a full consideration of available nucleation mechanisms; scenario 2 is set to probe the feasibility to use  
236 modified Kerminen-Kulmala equation to simulate the initial particle growth; scenario 3 is the “base-case” representing the  
237 performance of the original model; and scenario 4 represents the evolution of aerosol population only contributed by primary  
238 emission. Scenarios 3 and 4 were set as controlling groups to assess the role of SA-DMA nucleation and other mechanisms.

## 239 2.3 Ambient Measurements

240 Ambient observations were conducted at an urban site in Beijing from January 2018 to April 2018 and from October 2018 to  
241 March 2019. The site is located on the West Campus of Beijing University of Chemical Technology. Details of the observation  
242 site can be found in previous studies (Liu et al., 2020; Deng et al., 2020). The concentrations of SA and involving clusters are  
243 measured using a chemical ionization high resolution time of flight mass spectrometer (CI-HTOF-MS) and a chemical  
244 ionization time of flight mass spectrometer with a long mass analyzer (CI-LTOF-MS) (Bertram et al., 2011; Jokinen et al.,  
245 2012). Other details in the sampling configurations have been reported in our previous study (Deng et al., 2020). Amine  
246 concentrations are measured using a modified time of flight mass spectrometer (TOF-MS) (Zheng et al., 2015b; Cai et al.,  
247 2021b). A weather station was deployed to measure the meteorological data, including ambient temperature, relative humidity  
248 and pressure. The PNSDs of particles from 1 nm to 10  $\mu\text{m}$  were measured using a particle size distribution (PSD) and a diethyl  
249 glycol-scanning mobility particle sizer (DEG-SMPS) (Jiang et al., 2011; Liu et al., 2016; Cai et al., 2017a). CS is calculated  
250 from the measured PNSDs and  $J_{1,4}$  is calculated using an improved aerosol population balance formula (Cai and Jiang, 2017).  
251 The details of instrument calibrations and data validations can be found in our previous study (Cai et al., 2021b).

## 252 3 Results and discussion

### 253 3.1 Validation of Parameterization

254 The reasonability of pseudo-steady-state assumptions in the SA-DMA nucleation pathway was tested through comparisons  
255 between the e-folding time of cluster dynamics ( $\tau$ ) in the kinetic simulation (see details in the *SI*) and the time interval of  
256 observational data (30 min in this study). The characteristic equilibrium time of involving clusters and simulated  $J_{1,4}$  were  
257 shown in Fig. S1 in the *SI*. Generally, in either clean and cold circumstances or polluted and warm circumstances, the  
258 kinetically simulated  $J_{1,4}$  could be well reproduced by parameterized pseudo-steady-state  $J_{1,4}$ . Actually,  $\tau$  vary greatly with  
259 CoagS and  $\gamma$ , and would be higher on cleaner and colder days, while even in extremely clean and cold days with  $CS = 0.0001$   
260  $\text{s}^{-1}$  and  $T = 255$  K,  $\tau$  of  $A_3B_3$  (longer than other clusters) is only  $\sim 20$  min, shorter than the data collection time interval of 30  
261 min. Thus for circumstances where there are high atmospheric concentrations of DMA and SA, such as most typical polluted  
262 regions, we conclude that nucleation processes are rapid enough that kinetic  $J_{1,4}$  can be represented by pseudo-steady-state  $J_{1,4}$ .

263 Figure 1 presents the comparisons between parameterized  $J_{1,4}$  in this study and those simulated in the kinetic models (hereafter  
264 referred to as KM) presented by Cai et al. (2021) and the cluster dynamic simulations containing all  $A_mB_n$  ( $m, n \leq 4$ ) clusters  
265 (hereafter referred to as CDS). Generally, there are good consistencies the simulated  $J_{1,4}$  between KM and the parameterization  
266 with the correlation coefficient ( $R^2$ ) and normalized mean bias (NMB) of 0.9297 and 0.16, respectively. The simulated  $J_{1,4}$  in  
267 KM can be reproduced by parameterized  $J_{1,4}$  within a  $\pm 50\%$  range for most of the cases in urban Beijing, with no systematic  
268 deviations found between them.



269 Figure 1b shows that for most of the circumstances, deviations between the parameterized  $J_{1.4}$  and  $J_{1.4}$  simulated in CDS are  
270 within a range of 1 order of magnitude. The  $R^2$  and NMB of the simulated  $J_{1.4}$  between this parameterization and CDS are  
271 0.7244 and 0.29, respectively. However, for circumstances with high temperatures, the parameterized  $J_{1.4}$  were higher than  
272 those simulated in CDS, which might be due to that the  $A_kB_k$  ( $k=2,3$  and 4) clusters are assumed to be non-evaporative in KM  
273 while they would evaporate back in CDS under high temperatures. The reasonability of cluster stability assumptions under  
274 high temperatures relies mainly on the accuracy of quantum chemistry calculations, which requires more experimental  
275 evidence and discussions. Additionally, due to the negative dependence of simulated  $J_{1.4}$  on  $T$ , the simulated  $J_{1.4}$  in this  
276 parameterization were mostly lower than  $10 \text{ cm}^{-3}\text{s}^{-1}$  under temperatures higher than  $15 \text{ }^\circ\text{C}$ , lower than the median and mean  
277 value of particle formation rates measured during long-term observations in Beijing (Deng et al., 2021). Although they are  
278 relatively higher than those simulated in CDS, the simulation results of NPF occurrence did not show large deviations.

279 The computational costs of these three simulations have also been tested on the same personal computer with a Matlab program.  
280 To achieve the steady-state  $J_{1.4}$  in a specific atmospheric condition, the CDS and KM needs  $\sim 10 \text{ s}$  and  $\sim 0.05 \text{ s}$  CPU time,  
281 respectively, while the calculation of parameterized pseudo-steady-state  $J_{1.4}$  merely costs  $\sim 2 \times 10^{-7} \text{ s}$  CPU time. The CPU time  
282 was reduced by a factor of  $5 \times 10^7$  and  $4 \times 10^4$  compared to CDS and KM, respectively. Thus introducing this parameterization  
283 into 3-D chemical transport models could greatly reduce the computational costs.

### 284 3.2 The Dependence of Parameterized $J_{1.4}$ on Input Parameters

285 The correlation between parameterized SA-DMA nucleation  $J_{1.4}$  and the input parameters are shown in Fig. 2. The parameters  
286 involved are  $T$ , CS, [DMA], and [SA<sub>tot</sub>]. The mean values of measured data during the observation period (281K,  $0.02 \text{ s}^{-1}$ , 3  
287 ppt, and  $3.5 \times 10^6 \text{ cm}^{-3}$ , respectively) are applied as typical conditions in the base case. Different from the semi-empirical power-  
288 law functions only based on precursor concentrations presented by Dunne et al. (2016), the dependences of particle formation  
289 rates on  $T$  and CS are represented in our parameterizations. With  $T$  increasing from  $-10$  to  $20 \text{ }^\circ\text{C}$ ,  $\gamma$  would increase by  $\sim 2$  orders  
290 of magnitude, as shown in Fig. 2a, and thus  $J_{1.4}$  would decrease by over 2 orders of magnitude. This should be attributed to  
291 the positive dependence of evaporation rates of  $A_1B_1$  clusters on the temperature. Under circumstances with high temperatures,  
292 the formation of  $A_1B_1$  and subsequent formation of larger clusters and 1.4 nm particles would be suppressed. The decreasing  
293 trend of observed NPF rate ( $J_{1.5}$  in this case) as a function of increasing  $T$  in urban Beijing has also been reported (Deng et al.,  
294 2020), consistent with our parameterizations.

295 Fig. 2b shows that  $J_{1.4}$  would decrease by 2-4 orders of magnitude with CS increasing by a factor of 10, and the logarithm  
296 dependence is higher in circumstances with higher CS, such as urban Beijing, where CoagS dominates the sinks. This is  
297 consistent with the negative CS dependence of measured particle formation rates and NPF occurrence demonstrated in previous  
298 observations in Beijing (Deng et al., 2021; Cai et al., 2021b; Cai et al., 2021a). Note that the dependence of parameterized  $J_{1.4}$   
299 on CS is also sensitive to  $T$  due to the synergistic effect of evaporation and coagulation on the sink of  $A_1B_1$  clusters, which are  
300 the key species in SA-DMA nucleation (Cai et al., 2022). If temperatures are higher, evaporation would be the dominant sink  
301 of  $A_1B_1$  clusters while CS only suppresses the formation of larger clusters. While under lower temperatures, such as in  
302 wintertime Beijing, CS would be the dominant sink of both  $A_1B_1$  clusters and larger clusters.

303 The parameterized  $J_{1.4}$  shows an increasing trend with increasing concentrations of SA and DMA. The parameterized  $J_{1.4}$  is  
304 approximately proportional to [SA]<sup>4</sup>. This high dependence of parameterized  $J_{1.4}$  on [SA] could well reproduce the  
305 phenomenon that rapid formation of new particles usually occurs at noon, when there is usually strong formation of SA  
306 molecules in the atmosphere. The dependence of  $J_{1.4}$  on [DMA] is decreasing with increasing [DMA]. This is due to the near-  
307 saturation formation of  $A_1B_1$  clusters, which is also found in kinetic model simulation results (Cai et al., 2021d). Generally,  
308 the parameterization could reproduce the fact that SA-DMA nucleation is driven by SA-DMA cluster formation, dominantly  
309 suppressed by cluster evaporation and coagulation sinks.

### 310 3.3 Comparison of 3D Model Simulations with Observations

311 As [DMA], [SA] and CS are key input variables for the  $J_{1.4}$  parameterization, we first compare simulated [DMA], [SA] and  
312 CS from the DMA1.4\_Mech8 scenario with observations (Fig. 3). Generally, there are good consistencies of both mean values  
313 and temporal variations, although there are still deviations at certain times. The mean simulated [DMA], [SA], and CS are 1.9  
314 ppt,  $1.4 \times 10^6 \text{ cm}^{-3}$ , and  $0.040 \text{ s}^{-1}$ , respectively, close to observed values of 2.0 ppt,  $1.6 \times 10^6 \text{ cm}^{-3}$ , and  $0.043 \text{ s}^{-1}$ . In a quantitative  
315 view, the  $R^2$  between simulated and observed [DMA], [SA], and CS are 0.04, 0.37, and 0.40, respectively, while the  
316 coefficients during NPF periods increase to 0.12, 0.51, and 0.49. The normalized mean biases (NMBs) between simulated and  
317 observed [DMA], [SA], and CS are  $4.5 \times 10^{-3}$ , -0.22, and -0.36, respectively, while NMBs during NPF periods are -0.40, 0.01,  
318 and -0.66. Generally, the simulation of SA concentrations is good, especially during NPF periods with intense nucleation. We  
319 note that the correlation between simulated and observed DMA concentration is lower, which may be attributed to the large  
320 uncertainty of the diurnal variation of amine emission. Nevertheless, during NPF periods, the differences between the observed  
321 DMA concentration ( $0.78 \pm 0.60$  ppt) and our simulation ( $1.10 \pm 0.60$  ppt) is relatively small. For [SA] and CS, to which  $J_{1.4}$  are  
322 most sensitive, we compare the timeseries of simulated and observed  $[\text{SA}]^4/\text{CS}^2$  (based on the approximate dependence of  $J_{1.4}$   
323 on [SA] and CS, as shown in Fig. 2) during NPF periods to show the deviations of the combination of these two input parameters  
324 (Fig. S6). Generally, in most nucleation events, the simulated values would not deviate from the observed values by over an  
325 order of magnitude. This indicates the validity of the comprehensive representation of input parameters in the model.

326 The time series of PNSDs for different simulation scenarios are presented in Fig. 4. When SA-DMA nucleation is considered,  
327 the typical PNSDs shape in observed NPF days (12/07, 12/08, 12/09, 01/20, and 01/21), characterized as the burst of  
328 nanometer-sized particles and subsequent growth, are well captured by our “best-case” scenario DMA1.4\_Mech8 and also  
329 DMA1.7\_Mech8. By contrast, the scenarios without DMA-SA nucleation, NoDMA\_Mech7 and NoDMA\_Mech0, cannot  
330 reproduce the observed NPF events with a “vacancy band” for 1~10 nm size range over the entire simulation period. Actually,  
331 although there are slightly higher sub-3 nm particle concentrations in NoDMA\_Mech7 than those in NoDMA\_Mech0, which  
332 are generated from the 7 nucleation pathways other than DMA-SA nucleation, the newly formed particle concentrations are  
333 too low to survive in the subsequent growth and be separated from background aerosols in the PNSDs. These results  
334 demonstrate that SA-DMA nucleation should be the dominant mechanism during NPF events in Beijing compared with other  
335 7 mechanisms.

336 Our results also reproduce the dependence of NPF occurrence on CS in Beijing. As shown in Fig. S2 in the SI, NPF generally  
337 occurs at low CS while high CS results in too low nucleation rates to initiate NPF. The results were also validated through  
338 comparison between the timeseries of the simulated and observed CS (Fig. 3c). Note that the simulated sub-3 nm particle  
339 concentrations also increase slightly on some non-NPF days in DMA1.4\_Mech8 and DMA1.7\_Mech8 scenarios, however,  
340 the concentrations are ~1 order of magnitude lower than those on NPF days and the newly formed particles also fail to survive  
341 in the subsequent growth. The improvements of using the nucleation parameterization in this study is further stressed in the  
342 comparison between DMA1.4\_Mech8 scenario and the scenario (CLOUD) using the parameterization from Dunne et al.  
343 (2016). Figure S3 has shown that almost no rapid nucleation processes and NPF events are found in the simulation of CLOUD  
344 scenarios. In addition to the underestimation of nucleation rates, the simulated high nucleation rates usually occur on observed  
345 non-NPF days (Fig.S7), which should be attributed to the ignorance of CS dependence in the power-law function  
346 parameterizations.

347 Figure 5 further compares the simulated and observed PNSDs averaged over the simulation period. The “best-case” scenario  
348 DMA1.4\_Mech8 brings the averaged PNSD in 1~200 nm size range much closer to the observation than those of “base-case”  
349 NoDMA\_Mech7, and the latter only shows a minor change compared to scenario NoDMA\_Mech0 without any nucleation.  
350 One may notice that the averaged PNSD in 2~10 nm size range for scenario DMA1.4\_Mech8 is still lower than that of  
351 observation by ~1 order of magnitude, despite the good agreement in number concentrations of particles of ~1.4 nm. This

352 could be attributed to two possible reasons: the model underestimates the actual nucleation rates; or newly formed particles of  
353  $\sim 1.4$  nm grow too fast to larger size bins in the model ( $> 10$  nm). The first one can be excluded by a generally good agreement  
354 between simulated nucleation rates and ones derived from observation, even with a slightly higher mean value for the former  
355 (shown in next section, Fig. 6). The observation-simulation comparison of averaged PNSDs is further conducted for individual  
356 NPF days. As shown in Fig. S8, the simulated PNSDs on all NPF days follow a similar pattern as the two-month-averaged one  
357 in Fig. 6, indicating that nucleation in each simulated NPF day is accompanied by subsequent rapid growth. The difference in  
358 the concentration of 2-10 nm particles between observation and simulation is therefore a common feature on various days and  
359 is probably attributed to the simplified assumption in particle growth simulation. Hence, the gap in 2~10 nm size range might  
360 be attributed to the particle growth simulations in the model which deserves further improvement. Moreover, in spite of similar  
361 performance in improving PNSDs simulations compared to the “best-case” DMA1.4\_Mech8, the scenario of DMA1.7\_Mech8  
362 presents a shifted PNSD pattern to larger size range. For these two scenarios including SA-DMA nucleation, scenario  
363 DMA1.4\_Mech8 is more reasonable since a systematic underestimation exists over the entire 1~10 nm range in scenario  
364 DMA1.7\_Mech8. Still, the conversion from 1.4 nm rate to those for larger particles through modified Kerminen-Kulmala  
365 equation is an alternative way to depict SA-DMA nucleation for other models with different aerosol size settings. Overall,  
366 despite aforementioned deficiencies, our updated WRF-Chem/R2D-VBS model configured with the SA-DMA nucleation  
367 parameterization shows substantial improvement in representation of NPF events and the PNSD.

### 368 3.4 Contribution from Various Pathways to Nucleation Rates and Particle Number Concentrations

369 Quantitative analysis over various nucleation pathways is performed here to improve the understanding of NPF in Beijing. As  
370 presented in Fig. 6, the variation of nucleation rates, which are derived from observed PNSD data, is well represented by the  
371 best-case scenario DMA1.4\_Mech8. Compared to the vast majority contribution from SA-DMA nucleation, the nucleation  
372 rates from other nucleation mechanisms are lower by a factor of  $\sim 100$ . In addition, SA-DMA nucleation contributes over 60%  
373 to aerosol population, reinforcing its dominant role in modulating aerosol population in urban **atmospheres**.

### 374 3.5 Sensitivity Analysis

375 Having shown the significant improvement of model performance in simulating NPF by coupling the SA-DMA nucleation  
376 parameterization, we acknowledge that the simulation of SA-DMA nucleation in 3D model still has uncertainties in terms of  
377 both source-sink representation of DMA and nucleation parameterization. Here, several key factors which may alter model  
378 performance were selected to perform sensitivity analysis.

379 First, the uncertainties brought by  $\Delta G$  achieved from different quantum chemistry results are tested for both parameterized  $J_{1.4}$   
380 and the 3-D chemical transport model simulations. In previous studies, a number of  $\Delta G$  values have been reported: -11.02  
381 kcal mol<sup>-1</sup> (Ge et al., 2020b), -15.40 kcal mol<sup>-1</sup> (Ortega et al., 2012), -13.54 kcal mol<sup>-1</sup> (Myllys et al., 2019). The  $\Delta G$  of -14.00  
382 kcal mol<sup>-1</sup> was applied in (Cai et al., 2021d) to achieve good consistencies between simulated and measured  $J_{1.4}$  is also applied  
383 in the sensitivity analysis. Figure S9 shows the variation of parameterized  $J_{1.4}$  applying different  $\Delta G$  values at 281 K, the  
384 median temperature of the observation period. For DMA with median values of  $\sim 3$  ppt, different  $J_{1.4}$  could vary by  $\sim 5$  orders  
385 of magnitude with  $\Delta G$  between -11.02 kcal mol<sup>-1</sup> and -15.40 kcal mol<sup>-1</sup>, while  $J_{1.4}$  with  $\Delta G$  of -13.54 kcal mol<sup>-1</sup> is also lower  
386 than that of -15.40 kcal mol<sup>-1</sup> by a factor of  $\sim 10$ . However, if the DMA concentrations are up to  $\sim 30$  ppt, the differences of  $J_{1.4}$   
387 when  $\Delta G$  varies between -13.54 kcal mol<sup>-1</sup> and -15.40 kcal mol<sup>-1</sup> would become much smaller, due to the saturated formation  
388 of  $A_1B_1$  clusters. For the temperature of 298.15 K, the sensitivities of parameterized  $J_{1.4}$  are relatively larger, because the  
389 formation of  $A_1B_1$  clusters is far from saturation. Generally, the parameterized  $J_{1.4}$  could be very sensitive to different  $\Delta G$   
390 values achieved from quantum chemistry results due to the essential influence of cluster stabilities. As a result, using a lower  
391  $\Delta G$  value of -15.40 kcal mol<sup>-1</sup> in the 3-D simulations with the DMA1.4\_Mech8 scenario configuration could lead to much

392 higher nucleation rates compared to the observation (Fig. S10). Thus we call for a more systematic performance assessment  
393 of quantum chemistry calculation methods to constrain the uncertainties of cluster thermodynamic stabilities.

394 Moreover, for the DMA source, we conduct two sensitivity scenarios of doubling (DMA2) and halving (DMA0.5) the inputted  
395 DMA emission to test the influence of limited measurements in constraining the DMA/NH<sub>3</sub> emission ratio. As for the three  
396 sink processes, the parameters for DMA-•OH reaction and wet deposition reported in the literature have relatively small  
397 differences while aerosol uptake coefficient of DMA covers a wide range over two orders of magnitude. We then conduct two  
398 sensitivity scenarios using the upper ( $4.4 \times 10^{-2}$ , Upt4.4E-2) and lower ( $5.9 \times 10^{-4}$ , Upt5.9E-4) limit of aerosol uptake coefficient.  
399 All sensitivity scenarios are on the basis of the DMA1.4\_Mech8 configuration. The influence of scaled DMA emissions and  
400 varying uptake coefficients on simulated DMA concentration, PNSDs, and nucleation rate is shown in Fig. S11-S21 in the SI.  
401 As expected, the DMA concentration, especially for the nighttime spikes, is sensitive to the emission change. In DMA0.5, the  
402 simulated  $J$  are lower than those observed in almost all cases. In contrast, although the simulated  $J$  in DMA2 is on average  
403 higher than observations, they are comparable in some specific cases. Considering that during NPF cases, the observed [DMA]  
404 are averagely 1.4 times higher than those simulated in DMA1.4\_Mech8, we propose that the slight underestimation of DMA  
405 concentrations in this case might be the reason for underestimation in  $J$  in some cases. The sensitivity analysis for the uptake  
406 coefficient, however, shows different results. A higher uptake coefficient of  $4.4 \times 10^{-2}$  leads to a much lower DMA  
407 concentration (10% of the “best-case”) while DMA concentration only increase slightly when the lower limit of  $5.9 \times 10^{-4}$  is  
408 used. Moreover, the change in uptake coefficient show limited effect on PNSD. The reason is that the DMA concentrations  
409 during NPF periods are much less affected by the changes in uptake coefficient than those in non-NPF periods, since NPF  
410 usually occurs at low CS conditions when the uptake of DMA is weak.

411 The sensitivity analysis above show that the parameters used in our simulation are reasonable, since perturbations within the  
412 ranges reported in the literature generally worsen the model performance. We also expect more field measurements of DMA  
413 emission and its aerosol uptake to further constrain the key source-sink process parameters in the simulation of DMA, although  
414 some of them show minor effect on NPF and PNSD simulations.

#### 415 4 Conclusions

416 This study presents a dynamic-based SA-DMA nucleation parameterization for application in 3-D chemical transport models.  
417 Compared to the more widely-used semi-empirical power-law fitting parameterizations, this new parameterization is based on  
418 the key pathway of SA-DMA cluster formation and includes representations of the coagulation scavenging effect and cluster  
419 stability. Pseudo-steady-state assumptions were applied to reduced computational time and were validated according to the  
420 short characteristic equilibrium time and through comparisons with the cluster dynamic simulations and the kinetic model.  
421 Relative to simulating the SA-DMA nucleation with cluster dynamic simulations or the kinetic model, application of this new  
422 parameterization in 3-D chemical transport models greatly reduces the computational costs. We incorporated this new  
423 parameterization as well as the sources and sinks of DMA into the WRF-Chem/R2D-VBS model. Using the updated model,  
424 we simulated the DMA concentrations and PNSDs in Beijing during December 2018 and January 2019. Comparisons were  
425 made between 3-D model simulations and ambient measurements.

426 Good consistency was achieved in simulating the precursor concentrations, which validated the source-sink simulation of SA  
427 and DMA. Our quantitative analysis showed that compared to other nucleation mechanisms, SA-DMA nucleation contributed  
428 to >99% of particle formation rates and >60% of particle number concentrations during the simulation period in urban Beijing.  
429 Although the uncertainties exist due to the excess rapid growth in the 3-D simulations, SA-DMA nucleation should be a  
430 dominant sources of aerosol populations due to the dominant contribution to new particle formation rates. Further, the 3-D  
431 simulations with the new parameterization predicted the CS-dependent NPF occurrence in urban Beijing and quantitatively

432 reproduced the particle size distributions. These results demonstrated that incorporating the SA-DMA nucleation  
433 parameterization, including the effect of coagulation scavenging and cluster stabilities, with 3-D chemical transport models  
434 can significantly improve the simulation of NPF and the particle size distributions.

435 Our results demonstrated that 3-D simulations with a new SA-DMA parameterization could reproduce the CS-dependent  
436 particle formation rates and NPF occurrence observed in Beijing. Given that CS varies widely between NPF days and non-  
437 NPF days in urban **atmospheres** (Xiao et al., 2015; Wu et al., 2007; Deng et al., 2021), compared to semi-empirical power-law  
438 functions, this parameterization of particle formation rates is likely more effective in predicting the NPF occurrence in urban  
439 atmospheres. Additionally, the particle formation rates from other nucleation mechanisms should also be suppressed by high  
440 CS, which needs further exploration and parameterizations. Our methodology of applying pseudo-steady-state assumptions to  
441 kinetic models could be important in reducing computational costs of other SA-amine nucleation systems. For instance,  
442 quantum chemistry calculations indicate that other basic molecules like trimethylamine and diamines (Jen et al., 2016; Jen et  
443 al., 2014a), might also form relative stable clusters with SA molecules, hence the methodology of parameterizations in this  
444 study could be extended for them, or the basic molecules could also be treated as equivalent DMA concentrations. The  
445 improvements in model simulations of particle size distributions are important for improving simulations of cloud  
446 condensation nuclei and the climate effects of aerosols and NPF events. The improvements also provide more evidence for  
447 quantitatively evaluating **the environmental and health effect of newly-formed particles.**

448

#### 449 **Codes/Data availability**

450 The simulation output data and codes needed for figure reproduction have been posted on Github. The link is  
451 <https://github.com/laoyeyelao/new-SA-DMA-parameterization.git>.

#### 452 **Author Contribution**

453 Y.L., J.S., B.Z., and J.J. designed the research; J.Z., M.K., and J.J. collected the observational data; Y.L., R.C., and J.J. set up  
454 and tested the parameterization; J.S., B.Z., S.W., and D.G. developed the 3-D model and performed the simulations; Y.L. and  
455 J.S. analyzed the data with the help of R.C., B.Z., and J.J.; M.S. and Y.G. presented important suggestions for the writings;  
456 Y.L., J.S., B.Z., and J.J. wrote the paper with inputs from all co-authors.

#### 457 **Competing Interests**

458 Some authors are members of the editorial board of journal *Atmospheric Chemistry and Physics*. The peer-review process was  
459 guided by an independent editor, and the authors have also no other competing interests to declare.

#### 460 **Acknowledgement**

461 Financial support from the National Natural Science Foundation of China (22188102 and 42275110), Tencent Foundation  
462 through the XPLOER PRIZE and Samsung PM<sub>2.5</sub> SRP are acknowledged. M. Shrivastava acknowledges the support from  
463 the U.S. Department of Energy (DOE), Office of Science, Office of Biological and Environmental Research through the  
464 Early Career Research Program.

- 466 Almeida, J., Schobesberger, S., Kurten, A., Ortega, I. K., Kupiainen-Maatta, O., Praplan, A. P., Adamov, A., Amorim, A.,  
467 Bianchi, F., Breitenlechner, M., David, A., Dommen, J., Donahue, N. M., Downard, A., Dunne, E., Duplissy, J., Ehrhart, S.,  
468 Flagan, R. C., Franchin, A., Guida, R., Hakala, J., Hansel, A., Heinritzi, M., Henschel, H., Jokinen, T., Junninen, H., Kajos,  
469 M., Kangasluoma, J., Keskinen, H., Kupc, A., Kurten, T., Kvashin, A. N., Laaksonen, A., Lehtipalo, K., Leiminger, M., Leppa,  
470 J., Loukonen, V., Makhmutov, V., Mathot, S., McGrath, M. J., Nieminen, T., Olenius, T., Onnela, A., Petaja, T., Riccobono,  
471 F., Riipinen, I., Rissanen, M., Rondo, L., Ruuskanen, T., Santos, F. D., Sarnela, N., Schallhart, S., Schnitzhofer, R., Seinfeld,  
472 J. H., Simon, M., Sipila, M., Stozhkov, Y., Stratmann, F., Tome, A., Trostl, J., Tsagkogeorgas, G., Vaattovaara, P., Viisanen,  
473 Y., Virtanen, A., Vrtala, A., Wagner, P. E., Weingartner, E., Wex, H., Williamson, C., Wimmer, D., Ye, P. L., Yli-Juuti, T.,  
474 Carslaw, K. S., Kulmala, M., Curtius, J., Baltensperger, U., Worsnop, D. R., Vehkamäki, H., and Kirkby, J.: Molecular  
475 understanding of sulphuric acid-amine particle nucleation in the atmosphere, *Nature*, 502, 359-363, 2013.
- 476 Bergman, T., Laaksonen, A., Korhonen, H., Malila, J., Dunne, E. M., Mielonen, T., Lehtinen, K. E. J., Kuhn, T., Arola, A.,  
477 and Kokkola, H.: Geographical and diurnal features of amine-enhanced boundary layer nucleation, *J Geophys Res-Atmos*,  
478 120, 9606-9624, 2015.
- 479 Bertram, T. H., Kimmel, J. R., Crisp, T. A., Ryder, O. S., Yatavelli, R. L. N., Thornton, J. A., Cubison, M. J., Gonin, M., and  
480 Worsnop, D. R.: A field-deployable, chemical ionization time-of-flight mass spectrometer, *Atmos. Meas. Tech.*, 4, 1471-1479,  
481 10.5194/amt-4-1471-2011, 2011.
- 482 Cai, R., Chen, D.-R., Hao, J., and Jiang, J.: A miniature cylindrical differential mobility analyzer for sub-3 nm particle sizing,  
483 *Journal of Aerosol Science*, 106, 111-119, <https://doi.org/10.1016/j.jaerosci.2017.01.004>, 2017a.
- 484 Cai, R., Yan, C., Worsnop, D. R., Bianchi, F., Kerminen, V.-M., Liu, Y., Wang, L., Zheng, J., Kulmala, M., and Jiang, J.: An  
485 indicator for sulfuric acid-amine nucleation in atmospheric environments, *Aerosol Science and Technology*, 55, 1059-1069,  
486 10.1080/02786826.2021.1922598, 2021a.
- 487 Cai, R., Yan, C., Yang, D., Yin, R., Lu, Y., Deng, C., Fu, Y., Ruan, J., Li, X., Kontkanen, J., Zhang, Q., Kangasluoma, J., Ma,  
488 Y., Hao, J., Worsnop, D. R., Bianchi, F., Paasonen, P., Kerminen, V.-M., Liu, Y., Wang, L., Zheng, J., Kulmala, M., and Jiang,  
489 J.: Sulfuric acid-amine nucleation in urban Beijing, *Atmospheric Chemistry and Physics*, 21, 2457-2468, 10.5194/acp-21-  
490 2457-2021, 2021b.
- 491 Cai, R. L. and Jiang, J. K.: A new balance formula to estimate new particle formation rate: reevaluating the effect of coagulation  
492 scavenging, *Atmos Chem Phys*, 17, 12659-12675, 2017.
- 493 Cai, R. L., Yang, D. S., Fu, Y. Y., Wang, X., Li, X. X., Ma, Y., Hao, J. M., Zheng, J., and Jiang, J. K.: Aerosol surface area  
494 concentration: a governing factor in new particle formation in Beijing, *Atmos Chem Phys*, 17, 12327-12340, 2017b.
- 495 Cai, R. L., Yan, C., Worsnop, D. R., Bianchi, F., Kerminen, V. M., Liu, Y. C., Wang, L., Zheng, J., Kulmala, M., and Jiang,  
496 J. K.: An indicator for sulfuric acid-amine nucleation in atmospheric environments, *Aerosol Sci Tech*, 55, 1059-1069, 2021c.
- 497 Cai, R. L., Yan, C., Yang, D. S., Yin, R. J., Lu, Y. Q., Deng, C. J., Fu, Y. Y., Ruan, J. X., Li, X. X., Kontkanen, J., Zhang, Q.,  
498 Kangasluoma, J., Ma, Y., Hao, J. M., Worsnop, D. R., Bianchi, F., Paasonen, P., Kerminen, V. M., Liu, Y. C., Wang, L.,  
499 Zheng, J., Kulmala, M., and Jiang, J. K.: Sulfuric acid-amine nucleation in urban Beijing, *Atmos Chem Phys*, 21, 2457-2468,  
500 2021d.
- 501 Cai, R. L., Yin, R. J., Yan, C., Yang, D. S., Deng, C. J., Dada, L., Kangasluoma, J., Kontkanen, J., Halonen, R., Ma, Y., Zhang,  
502 X. H., Paasonen, P., Petaja, T., Kerminen, V. M., Liu, Y. C., Bianchi, F., Zheng, J., Wang, L., Hao, J. M., Smith, J. N., Donahue,  
503 N. M., Kulmala, M., Worsnop, D. R., and Jiang, J. K.: The missing base molecules in atmospheric acid-base nucleation, *Natl*  
504 *Sci Rev*, 9, 2022.
- 505 Chan, T. W. and Mozurkewich, M.: Measurement of the coagulation rate constant for sulfuric acid particles as a function of  
506 particle size using tandem differential mobility analysis, *J Aerosol Sci*, 32, 321-339, 2001.
- 507 Chen, D., Shen, Y., Wang, J., Gao, Y., Gao, H., and Yao, X.: Mapping gaseous dimethylamine, trimethylamine, ammonia,  
508 and their particulate counterparts in marine atmospheres of China's marginal seas – Part 1: Differentiating marine emission  
509 from continental transport, *Atmos Chem Phys*, 21, 16413-16425, 10.5194/acp-21-16413-2021, 2021a.
- 510 Chen, M., Titcombe, M., Jiang, J., Jen, C., Kuang, C., Fischer, M. L., Eisele, F. L., Siepmann, J. I., Hanson, D. R., Zhao, J.,  
511 and McMurry, P. H.: Acid-base chemical reaction model for nucleation rates in the polluted atmospheric boundary layer, *Proc*  
512 *Natl Acad Sci U S A*, 109, 18713-18718, 10.1073/pnas.1210285109, 2012.
- 513 Chen, X., Yang, W., Wang, Z., Li, J., Hu, M., An, J., Wu, Q., Wang, Z., Chen, H., Wei, Y., Du, H., and Wang, D.: Improving  
514 new particle formation simulation by coupling a volatility-basis set (VBS) organic aerosol module in NAQPMS+APM, *Atmos*  
515 *Environ*, 204, 1-11, <https://doi.org/10.1016/j.atmosenv.2019.01.053>, 2019.
- 516 Chen, X., Yu, F., Yang, W., Sun, Y., Chen, H., Du, W., Zhao, J., Wei, Y., Wei, L., Du, H., Wang, Z., Wu, Q., Li, J., An, J.,  
517 and Wang, Z.: Global-regional nested simulation of particle number concentration by combing microphysical processes with  
518 an evolving organic aerosol module, *Atmos. Chem. Phys.*, 21, 9343-9366, 10.5194/acp-21-9343-2021, 2021b.
- 519 Deng, C., Cai, R., Yan, C., Zheng, J., and Jiang, J.: Formation and growth of sub-3 nm particles in megacities: impact of  
520 background aerosols, *Faraday Discuss*, 226, 348-363, 10.1039/d0fd00083c, 2021.
- 521 Deng, C. J., Fu, Y. Y., Dada, L., Yan, C., Cai, R. L., Yang, D. S., Zhou, Y., Yin, R. J., Lu, Y. Q., Li, X. X., Qiao, X. H., Fan,  
522 X. L., Nie, W., Kontkanen, J., Kangasluoma, J., Chu, B. W., Ding, A. J., Kerminen, V. M., Paasonen, P., Worsnop, D. R.,  
523 Bianchi, F., Liu, Y. C., Zheng, J., Wang, L., Kulmala, M., and Jiang, J. K.: Seasonal Characteristics of New Particle Formation  
524 and Growth in Urban Beijing, *Environ Sci Technol*, 54, 8547-8557, 2020.
- 525 Dunne, E. M., Gordon, H., Kurten, A., Almeida, J., Duplissy, J., Williamson, C., Ortega, I. K., Pringle, K. J., Adamov, A.,  
526 Baltensperger, U., Barmet, P., Benduhn, F., Bianchi, F., Breitenlechner, M., Clarke, A., Curtius, J., Dommen, J., Donahue, N.  
527 M., Ehrhart, S., Flagan, R. C., Franchin, A., Guida, R., Hakala, J., Hansel, A., Heinritzi, M., Jokinen, T., Kangasluoma, J.,

528 Kirkby, J., Kulmala, M., Kupc, A., Lawler, M. J., Lehtipalo, K., Makhmutov, V., Mann, G., Mathot, S., Merikanto, J.,  
529 Miettinen, P., Nenes, A., Onnela, A., Rap, A., Reddington, C. L. S., Riccobono, F., Richards, N. A. D., Rissanen, M. P., Rondo,  
530 L., Sarnela, N., Schobesberger, S., Sengupta, K., Simon, M., Sipilaa, M., Smith, J. N., Stozkhov, Y., Tome, A., Trostl, J.,  
531 Wagner, P. E., Wimmer, D., Winkler, P. M., Worsnop, D. R., and Carslaw, K. S.: Global atmospheric particle formation from  
532 CERN CLOUD measurements, *Science*, 354, 1119-1124, 2016.

533 Ge, P., Luo, G., Huang, W., Xie, H., Chen, J., and Luo, Y.: Theoretical study of the hydration effects on alkylamine and  
534 alkanolamine clusters and the atmospheric implication, *Chemosphere*, 243, 125323,  
535 <https://doi.org/10.1016/j.chemosphere.2019.125323>, 2020a.

536 Ge, P., Luo, G., Huang, W., Xie, H. B., Chen, J. W., and Luo, Y.: Theoretical study of the hydration effects on alkylamine and  
537 alkanolamine clusters and the atmospheric implication, *Chemosphere*, 243, 2020b.

538 Ge, X., Wexler, A. S., and Clegg, S. L.: Atmospheric amines – Part I. A review, *Atmos Environ*, 45, 524-546,  
539 [10.1016/j.atmosenv.2010.10.012](https://doi.org/10.1016/j.atmosenv.2010.10.012), 2011.

540 Glasoe, W. A., Volz, K., Panta, B., Freshour, N., Bachman, R., Hanson, D. R., McMurry, P. H., and Jen, C.: Sulfuric acid  
541 nucleation: An experimental study of the effect of seven bases, *J Geophys Res-Atmos*, 120, 1933-1950, 2015.

542 Gordon, H., Kirkby, J., Baltensperger, U., Bianchi, F., Breitenlechner, M., Curtius, J., Dias, A., Dommen, J., Donahue, N. M.,  
543 Dunne, E. M., Duplissy, J., Ehrhart, S., Flagan, R. C., Frege, C., Fuchs, C., Hansel, A., Hoyle, C. R., Kulmala, M., Kurten, A.,  
544 Lehtipalo, K., Makhmutov, V., Molteni, U., Rissanen, M. P., Stozkhov, Y., Trostl, J., Tsagkogeorgas, G., Wagner, R.,  
545 Williamson, C., Wimmer, D., Winkler, P. M., Yan, C., and Carslaw, K. S.: Causes and importance of new particle formation  
546 in the present-day and preindustrial atmospheres, *J Geophys Res-Atmos*, 122, 8739-8760, 2017.

547 Guenther, A., Karl, T., Harley, P., Wiedinmyer, C., Palmer, P. I., and Geron, C.: Estimates of global terrestrial isoprene  
548 emissions using MEGAN (Model of Emissions of Gases and Aerosols from Nature), *Atmos. Chem. Phys.*, 6, 3181-3210,  
549 [10.5194/acp-6-3181-2006](https://doi.org/10.5194/acp-6-3181-2006), 2006.

550 Hanson, D. R., Bier, I., Panta, B., Jen, C. N., and McMurry, P. H.: Computational Fluid Dynamics Studies of a Flow Reactor:  
551 Free Energies of Clusters of Sulfuric Acid with NH<sub>3</sub> or Dimethyl Amine, *J Phys Chem A*, 121, 3976-3990, 2017.

552 Jen, C. N., McMurry, P. H., and Hanson, D. R.: Stabilization of sulfuric acid dimers by ammonia, methylamine, dimethylamine,  
553 and trimethylamine, *Journal of Geophysical Research: Atmospheres*, 119, 7502-7514, [10.1002/2014jd021592](https://doi.org/10.1002/2014jd021592), 2014a.

554 Jen, C. N., McMurry, P. H., and Hanson, D. R.: Stabilization of sulfuric acid dimers by ammonia, methylamine, dimethylamine,  
555 and trimethylamine, *J Geophys Res-Atmos*, 119, 7502-7514, 2014b.

556 Jen, C. N., Bachman, R., Zhao, J., McMurry, P. H., and Hanson, D. R.: Diamine-sulfuric acid reactions are a potent source of  
557 new particle formation, *Geophys Res Lett*, 43, 867-873, [10.1002/2015gl066958](https://doi.org/10.1002/2015gl066958), 2016.

558 Jiang, J., Chen, M., Kuang, C., Attoui, M., and McMurry, P. H.: Electrical Mobility Spectrometer Using a Diethylene Glycol  
559 Condensation Particle Counter for Measurement of Aerosol Size Distributions Down to 1 nm, *Aerosol Science and Technology*,  
560 45, 510-521, [10.1080/02786826.2010.547538](https://doi.org/10.1080/02786826.2010.547538), 2011.

561 Jokinen, T., Sipilä M., Junninen, H., Ehn, M., Lönn, G., Hakala, J., Petäjä T., Mauldin Iii, R. L., Kulmala, M., and Worsnop,  
562 D. R.: Atmospheric sulphuric acid and neutral cluster measurements using CI-API-TOF, *Atmos. Chem. Phys.*, 12, 4117-4125,  
563 [10.5194/acp-12-4117-2012](https://doi.org/10.5194/acp-12-4117-2012), 2012.

564 Kulmala, M.: How particles nucleate and grow, *Science*, 302, 1000-1001, 2003.

565 Kulmala, M., Vehkamäki, H., Petaja, T., Dal Maso, M., Lauri, A., Kerminen, V. M., Birmili, W., and McMurry, P. H.:  
566 Formation and growth rates of ultrafine atmospheric particles: a review of observations, *J Aerosol Sci*, 35, 143-176, 2004.

567 Kurten, A., Li, C. X., Bianchi, F., Curtius, J., Dias, A., Donahue, N. M., Duplissy, J., Flagan, R. C., Hakala, J., Jokinen, T.,  
568 Kirkby, J., Kulmala, M., Laaksonen, A., Lehtipalo, K., Makhmutov, V., Onnela, A., Rissanen, M. P., Simon, M., Sipila, M.,  
569 Stozkhov, Y., Trostl, J., Ye, P. L., and McMurry, P. H.: New particle formation in the sulfuric acid-dimethylamine-water  
570 system: reevaluation of CLOUD chamber measurements and comparison to an aerosol nucleation and growth model, *Atmos*  
571 *Chem Phys*, 18, 845-863, 2018.

572 Kurten, A., Jokinen, T., Simon, M., Sipila, M., Sarnela, N., Junninen, H., Adamov, A., Almeida, J., Amorim, A., Bianchi, F.,  
573 Breitenlechner, M., Dommen, J., Donahue, N. M., Duplissy, J., Ehrhart, S., Flagan, R. C., Franchin, A., Hakala, J., Hansel, A.,  
574 Heinritzi, M., Hutterli, M., Kangasluoma, J., Kirkby, J., Laaksonen, A., Lehtipalo, K., Leiminger, M., Makhmutov, V., Mathot,  
575 S., Onnela, A., Petaja, T., Praplan, A. P., Riccobono, F., Rissanen, M. P., Rondo, L., Schobesberger, S., Seinfeld, J. H., Steiner,  
576 G., Tome, A., Trostl, J., Winkler, P. M., Williamson, C., Wimmer, D., Ye, P. L., Baltensperger, U., Carslaw, K. S., Kulmala,  
577 M., Worsnop, D. R., and Curtius, J.: Neutral molecular cluster formation of sulfuric acid-dimethylamine observed in real time  
578 under atmospheric conditions, *P Natl Acad Sci USA*, 111, 15019-15024, 2014.

579 Lehtinen, K. E. J., Dal Maso, M., Kulmala, M., and Kerminen, V. M.: Estimating nucleation rates from apparent particle  
580 formation rates and vice versa: Revised formulation of the Kerminen-Kulmala equation, *J Aerosol Sci*, 38, 988-994, 2007.

581 Lehtipalo, K., Rondo, L., Kontkanen, J., Schobesberger, S., Jokinen, T., Sarnela, N., Kurten, A., Ehrhart, S., Franchin, A.,  
582 Nieminen, T., Riccobono, F., Sipila, M., Yli-Juuti, T., Duplissy, J., Adamov, A., Ahlm, L., Almeida, J., Amorim, A., Bianchi,  
583 F., Breitenlechner, M., Dommen, J., Downard, A. J., Dunne, E. M., Flagan, R. C., Guida, R., Hakala, J., Hansel, A., Jud, W.,  
584 Kangasluoma, J., Kerminen, V. M., Keskinen, H., Kim, J., Kirkby, J., Kupc, A., Kupiainen-Maatta, O., Laaksonen, A., Lawler,  
585 M. J., Leiminger, M., Mathot, S., Olenius, T., Ortega, I. K., Onnela, A., Petaja, T., Praplan, A., Rissanen, M. P., Ruuskanen,  
586 T., Santos, F. D., Schallhart, S., Schnitzhofer, R., Simon, M., Smith, J. N., Trostl, J., Tsagkogeorgas, G., Tome, A., Vaattovaara,  
587 P., Vehkamäki, H., Vrtala, A. E., Wagner, P. E., Williamson, C., Wimmer, D., Winkler, P. M., Virtanen, A., Donahue, N. M.,  
588 Carslaw, K. S., Baltensperger, U., Riipinen, I., Curtius, J., Worsnop, D. R., and Kulmala, M.: The effect of acid-base clustering  
589 and ions on the growth of atmospheric nano-particles, *Nat Commun*, 7, 2016.

590 Li, M., Zhang, Q., Kurokawa, J. I., Woo, J. H., He, K., Lu, Z., Ohara, T., Song, Y., Streets, D. G., Carmichael, G. R., Cheng,  
591 Y., Hong, C., Huo, H., Jiang, X., Kang, S., Liu, F., Su, H., and Zheng, B.: MIX: a mosaic Asian anthropogenic emission

592 inventory under the international collaboration framework of the MICS-Asia and HTAP, *Atmos. Chem. Phys.*, 17, 935-963,  
593 10.5194/acp-17-935-2017, 2017.

594 Liu, J., Jiang, J., Zhang, Q., Deng, J., and Hao, J.: A spectrometer for measuring particle size distributions in the range of 3  
595 nm to 10  $\mu$ m, *Frontiers of Environmental Science & Engineering*, 10, 63-72, 10.1007/s11783-014-0754-x, 2016.

596 Liu, L., Yu, F., Du, L., Yang, Z., Francisco, J. S., and Zhang, X.: Rapid sulfuric acid–dimethylamine nucleation enhanced by  
597 nitric acid in polluted regions, *Proceedings of the National Academy of Sciences*, 118, e2108384118,  
598 10.1073/pnas.2108384118, 2021.

599 Liu, Y., Yan, C., Feng, Z., Zheng, F., Fan, X., Zhang, Y., Li, C., Zhou, Y., Lin, Z., Guo, Y., Zhang, Y., Ma, L., Zhou, W., Liu,  
600 Z., Dada, L., Dällenbach, K., Kontkanen, J., Cai, R., Chan, T., Chu, B., Du, W., Yao, L., Wang, Y., Cai, J., Kangasluoma, J.,  
601 Kokkonen, T., Kujansuu, J., Rusanen, A., Deng, C., Fu, Y., Yin, R., Li, X., Lu, Y., Liu, Y., Lian, C., Yang, D., Wang, W., Ge,  
602 M., Wang, Y., Worsnop, D. R., Junninen, H., He, H., Kerminen, V.-M., Zheng, J., Wang, L., Jiang, J., Petäjä T., Bianchi, F.,  
603 and Kulmala, M.: Continuous and comprehensive atmospheric observations in Beijing: a station to understand the complex  
604 urban atmospheric environment, *Big Earth Data*, 4, 295-321, 10.1080/20964471.2020.1798707, 2020.

605 Lu, Y. Q., Liu, L., Ning, A., Yang, G., Liu, Y. L., Kurten, T., Vehkamäki, H., Zhang, X. H., and Wang, L.: Atmospheric  
606 Sulfuric Acid-Dimethylamine Nucleation Enhanced by Trifluoroacetic Acid, *Geophys Res Lett*, 47, 2020.

607 Mao, J., Yu, F., Zhang, Y., An, J., Wang, L., Zheng, J., Yao, L., Luo, G., Ma, W., Yu, Q., Huang, C., Li, L., and Chen, L.:  
608 High-resolution modeling of gaseous methylamines over a polluted region in China: source-dependent emissions and  
609 implications of spatial variations, *Atmospheric Chemistry and Physics*, 18, 7933-7950, 10.5194/acp-18-7933-2018, 2018.

610 Marten, R., Xiao, M., Rörup, B., Wang, M., Kong, W., He, X.-C., Stolzenburg, D., Pfeifer, J., Marie, G., Wang, D. S., Scholz,  
611 W., Baccharini, A., Lee, C. P., Amorim, A., Baalbaki, R., Bell, D. M., Bertozzi, B., Caudillo, L., Chu, B., Dada, L., Duplissy,  
612 J., Finkenzeller, H., Carracedo, L. G., Granzin, M., Hansel, A., Heinritzi, M., Hofbauer, V., Kempainen, D., Kürten, A.,  
613 Lampimäki, M., Lehtipalo, K., Makhmutov, V., Manninen, H. E., Mentler, B., Petäjä T., Philippov, M., Shen, J., Simon, M.,  
614 Stozhkov, Y., Tomé A., Wagner, A. C., Wang, Y., Weber, S. K., Wu, Y., Zauner-Wieczorek, M., Curtius, J., Kulmala, M.,  
615 Möhler, O., Volkamer, R., Winkler, P. M., Worsnop, D. R., Dommen, J., Flagan, R. C., Kirkby, J., Donahue, N. M.,  
616 Lamkaddam, H., Baltensperger, U., and El Haddad, I.: Survival of newly formed particles in haze conditions, *Environmental*  
617 *Science: Atmospheres*, 2, 491-499, 10.1039/D2EA00007E, 2022.

618 McGrath, M. J., Olenius, T., Ortega, I. K., Loukonen, V., Paasonen, P., Kurten, T., Kulmala, M., and Vehkamäki, H.:  
619 Atmospheric Cluster Dynamics Code: a flexible method for solution of the birth-death equations, *Atmos Chem Phys*, 12, 2345-  
620 2355, 2012.

621 Merikanto, J., Spracklen, D. V., Mann, G. W., Pickering, S. J., and Carslaw, K. S.: Impact of nucleation on global CCN, *Atmos*  
622 *Chem Phys*, 9, 8601-8616, 2009.

623 Mylly, N., Kubecka, J., Besel, V., Alfaouri, D., Olenius, T., Smith, J. N., and Passananti, M.: Role of base strength, cluster  
624 structure and charge in sulfuric-acid-driven particle formation, *Atmos Chem Phys*, 19, 9753-9768, 2019.

625 Olenius, T., Kupiainen-Maatta, O., Ortega, I. K., Kurten, T., and Vehkamäki, H.: Free energy barrier in the growth of sulfuric  
626 acid-ammonia and sulfuric acid-dimethylamine clusters, *J Chem Phys*, 139, 2013.

627 Olenius, T., Halonen, R., Kurten, T., Henschel, H., Kupiainen-Maatta, O., Ortega, I. K., Jen, C. N., Vehkamäki, H., and Riipinen,  
628 I.: New particle formation from sulfuric acid and amines: Comparison of monomethylamine, dimethylamine, and  
629 trimethylamine, *J Geophys Res-Atmos*, 122, 7103-7118, 2017.

630 Ortega, I. K., Kupiainen, O., Kurten, T., Olenius, T., Wilkman, O., McGrath, M. J., Loukonen, V., and Vehkamäki, H.: From  
631 quantum chemical formation free energies to evaporation rates, *Atmos Chem Phys*, 12, 225-235, 2012.

632 Qiu, C., Wang, L., Lal, V., Khalizov, A. F., and Zhang, R.: Heterogeneous reactions of alkylamines with ammonium sulfate  
633 and ammonium bisulfate, *Environ Sci Technol*, 45, 4748-4755, 10.1021/es1043112, 2011.

634 Riccobono, F., Schobesberger, S., Scott, C. E., Dommen, J., Ortega, I. K., Rondo, L., Almeida, J., Amorim, A., Bianchi, F.,  
635 Breitenlechner, M., David, A., Downard, A., Dunne, E. M., Duplissy, J., Ehrhart, S., Flagan, R. C., Franchin, A., Hansel, A.,  
636 Junninen, H., Kajos, M., Keskinen, H., Kupc, A., Kurten, A., Kvashin, A. N., Laaksonen, A., Lehtipalo, K., Makhmutov, V.,  
637 Mathot, S., Nieminen, T., Onnela, A., Petaja, T., Praplan, A. P., Santos, F. D., Schallhart, S., Seinfeld, J. H., Sipila, M.,  
638 Spracklen, D. V., Stozhkov, Y., Stratmann, F., Tome, A., Tsagkogeorgas, G., Vaattovaara, P., Viisanen, Y., Vrtala, A., Wagner,  
639 P. E., Weingartner, E., Wex, H., Wimmer, D., Carslaw, K. S., Curtius, J., Donahue, N. M., Kirkby, J., Kulmala, M., Worsnop,  
640 D. R., and Baltensperger, U.: Oxidation Products of Biogenic Emissions Contribute to Nucleation of Atmospheric Particles,  
641 *Science*, 344, 717-721, 2014.

642 Scaets, M. G.: Brownian coagulation in aerosols—the role of long range forces, *J Colloid Interf Sci*, 129, 105-112,  
643 [https://doi.org/10.1016/0021-9797\(89\)90419-0](https://doi.org/10.1016/0021-9797(89)90419-0), 1989.

644 Seinfeld, J. H. and Pandis, S. N.: *Atmospheric Chemistry and Physics: From Air Pollution to Climate Change*, 1998.

645 Semeniuk, K. and Dastoor, A.: Current state of aerosol nucleation parameterizations for air-quality and climate modeling,  
646 *Atmos Environ*, 179, 77-106, 2018.

647 Shrivastava, M., Fast, J., Easter, R., Gustafson Jr, W. I., Zaveri, R. A., Jimenez, J. L., Saide, P., and Hodzic, A.: Modeling  
648 organic aerosols in a megacity: comparison of simple and complex representations of the volatility basis set approach, *Atmos.*  
649 *Chem. Phys.*, 11, 6639-6662, 10.5194/acp-11-6639-2011, 2011.

650 Shrivastava, M., Andreae, M. O., Artaxo, P., Barbosa, H. M. J., Berg, L. K., Brito, J., Ching, J., Easter, R. C., Fan, J., Fast, J.  
651 D., Feng, Z., Fuentes, J. D., Glasius, M., Goldstein, A. H., Alves, E. G., Gomes, H., Gu, D., Guenther, A., Jathar, S. H., Kim,  
652 S., Liu, Y., Lou, S., Martin, S. T., McNeill, V. F., Medeiros, A., de Sá S. S., Shilling, J. E., Springston, S. R., Souza, R. A. F.,  
653 Thornton, J. A., Isaacman-VanWertz, G., Yee, L. D., Ynoue, R., Zaveri, R. A., Zelenyuk, A., and Zhao, C.: Urban pollution  
654 greatly enhances formation of natural aerosols over the Amazon rainforest, *Nat Commun*, 10, 1046, 10.1038/s41467-019-  
655 08909-4, 2019.



656 Stolzenburg, D., Simon, M., Ranjithkumar, A., Kürten, A., Lehtipalo, K., Gordon, H., Ehrhart, S., Finkenzeller, H.,  
657 Pichelstorfer, L., Nieminen, T., He, X.-C., Brilke, S., Xiao, M., Amorim, A., Baalbaki, R., Baccarini, A., Beck, L., Bräkling,  
658 S., Caudillo Murillo, L., Chen, D., Chu, B., Dada, L., Dias, A., Dommen, J., Duplissy, J., El Haddad, I., Fischer, L., Gonzalez  
659 Carracedo, L., Heinritzi, M., Kim, C., Koenig, T. K., Kong, W., Lamkaddam, H., Lee, C. P., Leiminger, M., Li, Z., Makhmutov,  
660 V., Manninen, H. E., Marie, G., Marten, R., Müller, T., Nie, W., Partoll, E., Petäjä T., Pfeifer, J., Philippov, M., Rissanen, M.  
661 P., Rörup, B., Schobesberger, S., Schuchmann, S., Shen, J., Sipilä M., Steiner, G., Stozhkov, Y., Tauber, C., Tham, Y. J.,  
662 Tomé A., Vazquez-Pufleau, M., Wagner, A. C., Wang, M., Wang, Y., Weber, S. K., Wimmer, D., Wlasits, P. J., Wu, Y., Ye,  
663 Q., Zauner-Wieczorek, M., Baltensperger, U., Carslaw, K. S., Curtius, J., Donahue, N. M., Flagan, R. C., Hansel, A., Kulmala,  
664 M., Lelieveld, J., Volkamer, R., Kirkby, J., and Winkler, P. M.: Enhanced growth rate of atmospheric particles from sulfuric  
665 acid, *Atmos Chem Phys*, 20, 7359-7372, 10.5194/acp-20-7359-2020, 2020.

666 Wang, L., Lal, V., Khalizov, A. F., and Zhang, R.: Heterogeneous Chemistry of Alkylamines with Sulfuric Acid: Implications  
667 for Atmospheric Formation of Alkylammonium Sulfates, *Environmental Science & Technology*, 44, 2461-2465,  
668 10.1021/es9036868, 2010.

669 Wang, Z.-Q., Liu, Y.-R., Wang, C.-Y., Jiang, S., Feng, Y.-J., Huang, T., and Huang, W.: Multicomponent nucleation of  
670 malonic acid involved in the sulfuric acid - dimethylamine system and its atmospheric implications, *Atmos Environ*, 267,  
671 118558, <https://doi.org/10.1016/j.atmosenv.2021.118558>, 2021.

672 Wu, Z. J., Hu, M., Liu, S., Wehner, B., Bauer, S., Ssling, A. M., Wiedensohler, A., Petaja, T., Dal Maso, M., and Kulmala,  
673 M.: New particle formation in Beijing, China: Statistical analysis of a 1-year data set, *J Geophys Res-Atmos*, 112, 2007.

674 Xiao, S., Wang, M. Y., Yao, L., Kulmala, M., Zhou, B., Yang, X., Chen, J. M., Wang, D. F., Fu, Q. Y., Worsnop, D. R., and  
675 Wang, L.: Strong atmospheric new particle formation in winter in urban Shanghai, China, *Atmospheric Chemistry and Physics*,  
676 15, 1769-1781, 10.5194/acp-15-1769-2015, 2015.

677 Yang, D., Zhu, S., Ma, Y., Zhou, L., Zheng, F., Wang, L., Jiang, J., and Zheng, J.: Emissions of Ammonia and Other Nitrogen-  
678 Containing Volatile Organic Compounds from Motor Vehicles under Low-Speed Driving Conditions, *Environmental Science  
& Technology*, 56, 5440-5447, 10.1021/acs.est.2c00555, 2022.

680 Yang, S., Liu, Z., Clusius, P. S., Liu, Y., Zou, J., Yang, Y., Zhao, S., Zhang, G., Xu, Z., Ma, Z., Yang, Y., Sun, J., Pan, Y., Ji,  
681 D., Hu, B., Yan, C., Boy, M., Kulmala, M., and Wang, Y.: Chemistry of new particle formation and growth events during  
682 wintertime in suburban area of Beijing: Insights from highly polluted atmosphere, *Atmospheric Research*, 255, 105553,  
683 <https://doi.org/10.1016/j.atmosres.2021.105553>, 2021.

684 Yao, L., Garmash, O., Bianchi, F., Zheng, J., Yan, C., Kontkanen, J., Junninen, H., Mazon, S. B., Ehn, M., Paasonen, P., Sipilä,  
685 M., Wang, M. Y., Wang, X. K., Xiao, S., Chen, H. F., Lu, Y. Q., Zhang, B. W., Wang, D. F., Fu, Q. Y., Geng, F. H., Li, L.,  
686 Wang, H. L., Qiao, L. P., Yang, X., Chen, J. M., Kerminen, V. M., Petaja, T., Worsnop, D. R., Kulmala, M., and Wang, L.:  
687 Atmospheric new particle formation from sulfuric acid and amines in a Chinese megacity, *Science*, 361, 278-281, 2018.

688 Yin, R., Yan, C., Cai, R., Li, X., Shen, J., Lu, Y., Schobesberger, S., Fu, Y., Deng, C., Wang, L., Liu, Y., Zheng, J., Xie, H.,  
689 Bianchi, F., Worsnop, D. R., Kulmala, M., and Jiang, J.: Acid-Base Clusters during Atmospheric New Particle Formation in  
690 Urban Beijing, *Environmental Science & Technology*, 55, 10994-11005, 10.1021/acs.est.1c02701, 2021.

691 Yu, F.: From molecular clusters to nanoparticles: second-generation ion-mediated nucleation model, *Atmos Chem Phys*, 6,  
692 5193-5211, 2006.

693 Yu, F. Q. and Turco, R. P.: From molecular clusters to nanoparticles: Role of ambient ionization in tropospheric aerosol  
694 formation, *J Geophys Res-Atmos*, 106, 4797-4814, 2001.

695 Zaveri, R. A., Easter, R. C., Shilling, J. E., and Seinfeld, J. H.: Modeling kinetic partitioning of secondary organic aerosol and  
696 size distribution dynamics: representing effects of volatility, phase state, and particle-phase reaction, *Atmos Chem Phys*, 14,  
697 5153-5181, 2014.

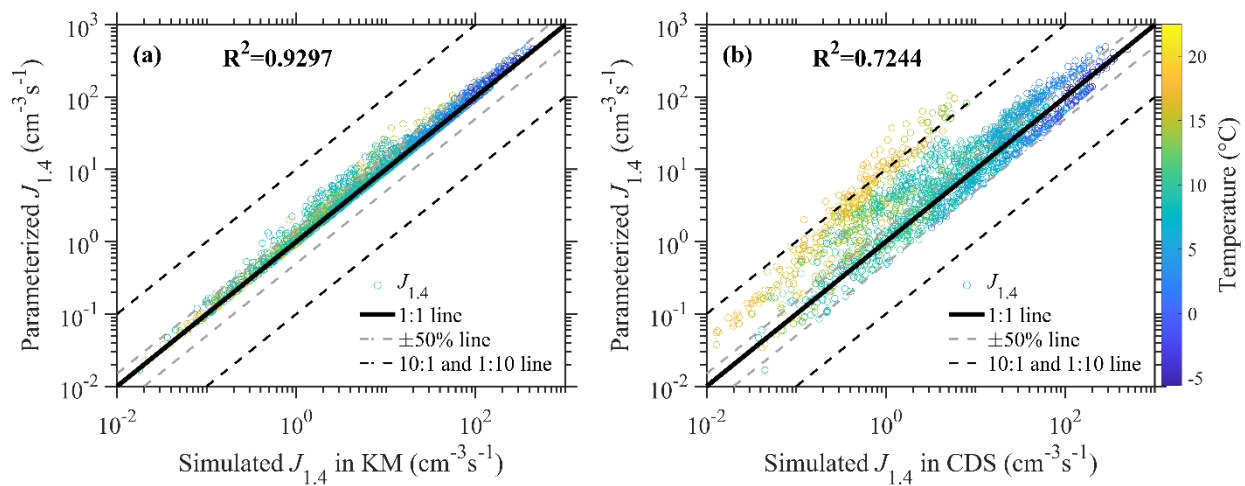
698 Zhao, B., Shrivastava, M., Donahue, N. M., Gordon, H., Schervish, M., Shilling, J. E., Zaveri, R. A., Wang, J., Andreae, M.  
699 O., Zhao, C., Gaudet, B., Liu, Y., Fan, J., and Fast, J. D.: High concentration of ultrafine particles in the Amazon free  
700 troposphere produced by organic new particle formation, *Proc Natl Acad Sci U S A*, 117, 25344-25351,  
701 10.1073/pnas.2006716117, 2020.

702 Zheng, H., Cai, S., Wang, S., Zhao, B., Chang, X., and Hao, J.: Development of a unit-based industrial emission inventory in  
703 the Beijing-Tianjin-Hebei region and resulting improvement in air quality modeling, *Atmospheric Chemistry and Physics*, 19,  
704 3447-3462, 10.5194/acp-19-3447-2019, 2019.

705 Zheng, J., Ma, Y., Chen, M., Zhang, Q., Wang, L., Khalizov, A. F., Yao, L., Wang, Z., Wang, X., and Chen, L.: Measurement  
706 of atmospheric amines and ammonia using the high resolution time-of-flight chemical ionization mass spectrometry, *Atmos  
Environ*, 102, 249-259, 10.1016/j.atmosenv.2014.12.002, 2015a.

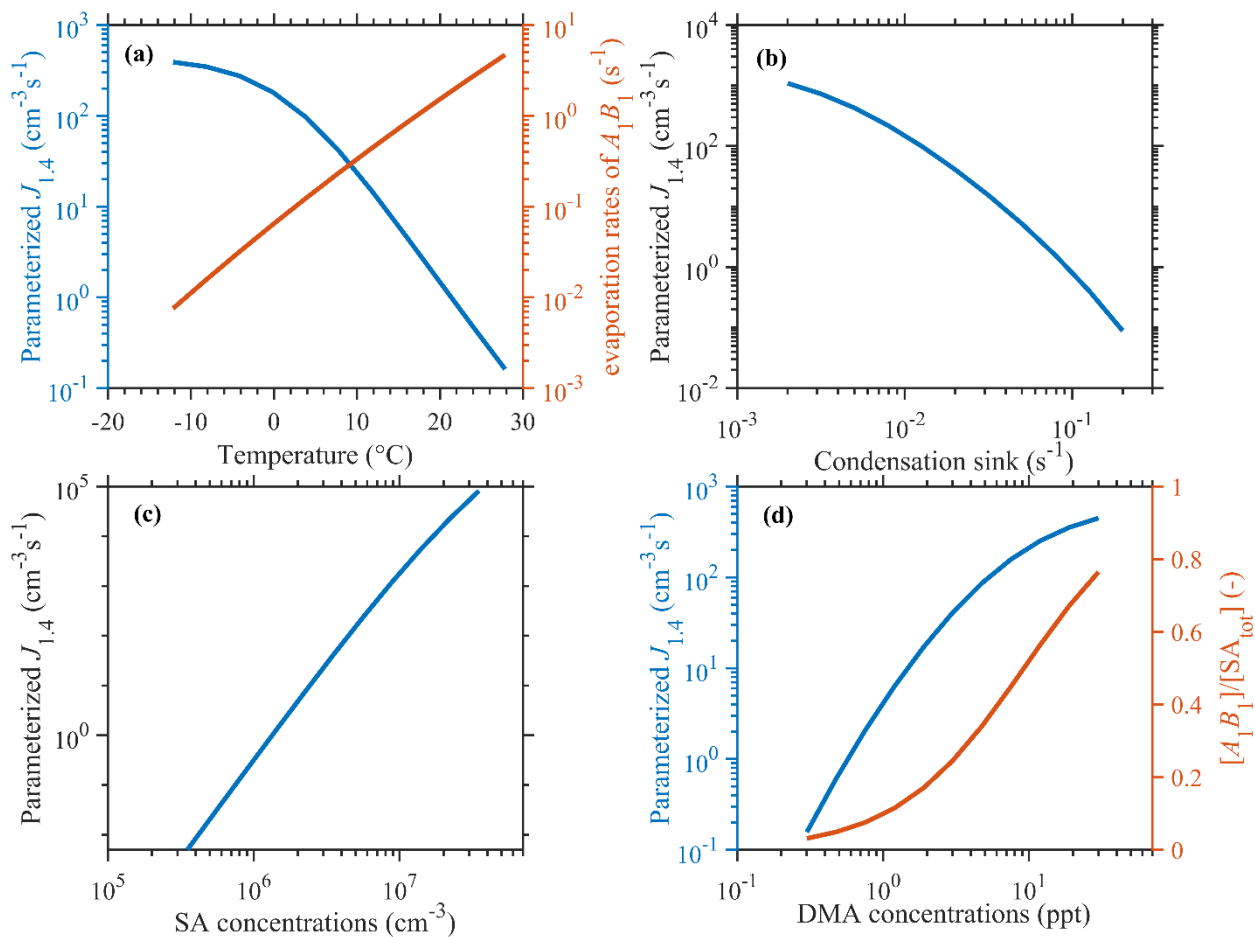
708 Zheng, J., Ma, Y., Chen, M. D., Zhang, Q., Wang, L., Khalizov, A. F., Yao, L., Wang, Z., Wang, X., and Chen, L. X.:  
709 Measurement of atmospheric amines and ammonia using the high resolution time-of-flight chemical ionization mass  
710 spectrometry, *Atmos Environ*, 102, 249-259, 2015b.

711 Zhu, S., Yan, C., Zheng, J., Chen, C., Ning, H., Yang, D., Wang, M., Ma, Y., Zhan, J., Hua, C., Yin, R., Li, Y., Liu, Y., Jiang,  
712 J., Yao, L., Wang, L., Kulmala, M., and Worsnop, D. R.: Observation and Source Apportionment of Atmospheric Alkaline  
713 Gases in Urban Beijing, *Environmental Science & Technology*, 56, 17545-17555, 10.1021/acs.est.2c03584, 2022.



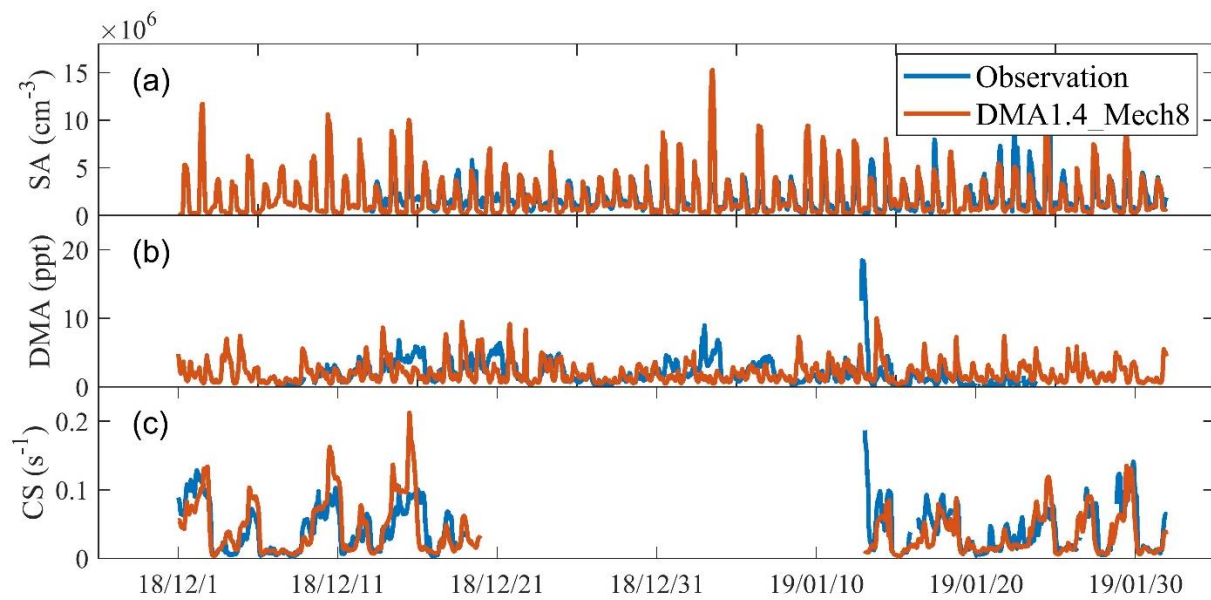
716

717 **Figure 1.  $J_{1,4}$  Comparison of simplified parameterization method with kinetic model (KM) results (a) and cluster**  
 718 **dynamic simulation (CDS) results (b).** The red hollow circles showed the simulation results according to atmospheric  
 719 observation data. The grey straight line represents the 1:1 line, while the grey dashed line represents the  $\pm 50\%$  variation and  
 720 the black dashed lines represent 1:10 or 10:1 line. The circles are colored by the temperatures.



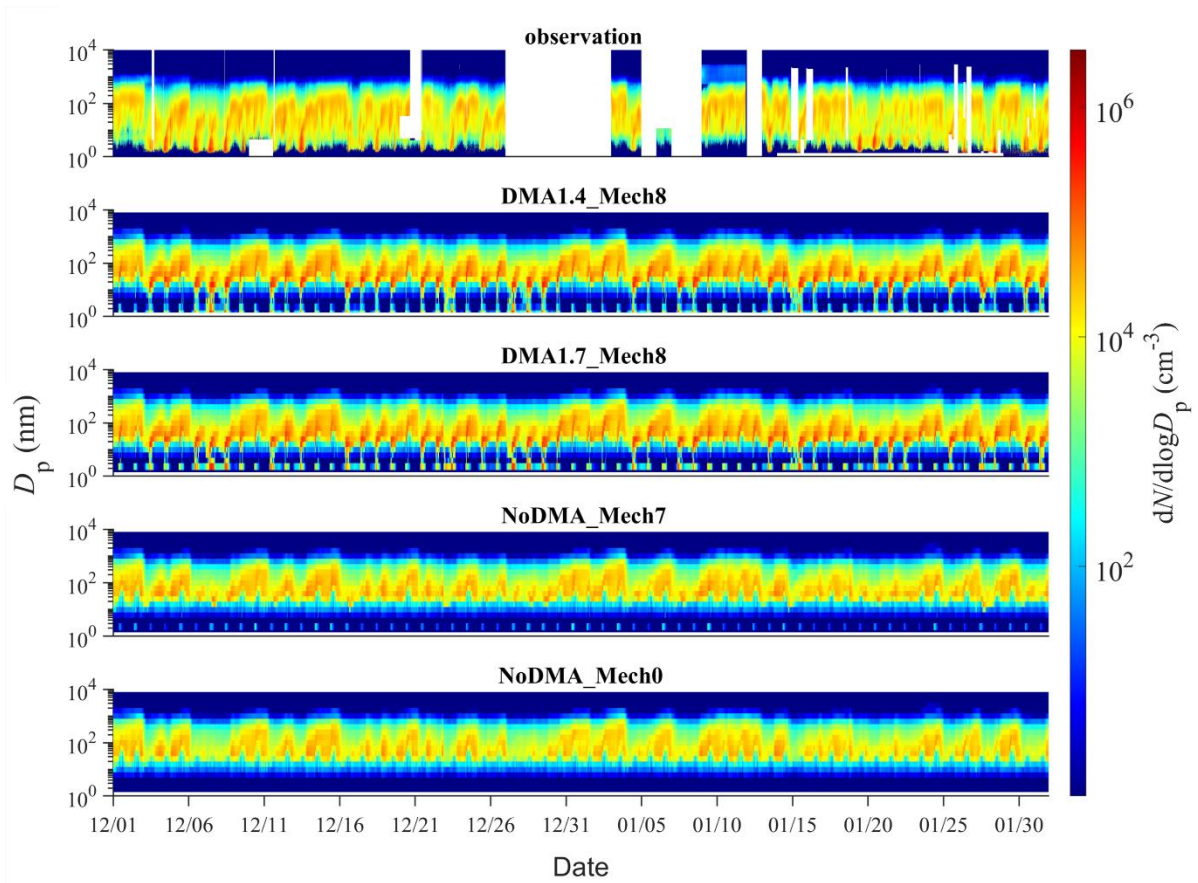
721

722 **Figure 2. Dependence of simulation results on varying  $T$ ,  $CS$ ,  $[DMA]$ ,  $[SA]$ .** The values of fixed parameters are 281K, 0.02  
 723  $\text{s}^{-1}$ , 3 ppt, and  $3.5 \times 10^6\text{ cm}^{-3}$ , respectively, as median values during NPF events in our simulation period.



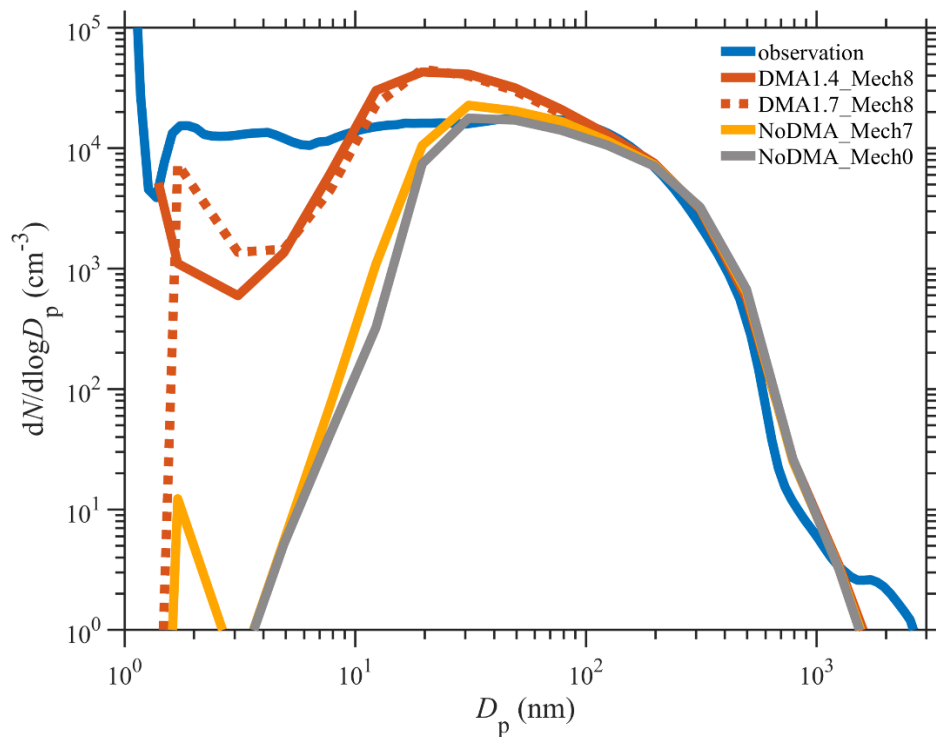
724

725 **Figure 3. Comparison of simulated concentrations of DMA (a), SA (b), and CS during periods with full PNSD**  
 726 **observation (c) with field measurements for wintertime Beijing (December 2018 and January 2019).**



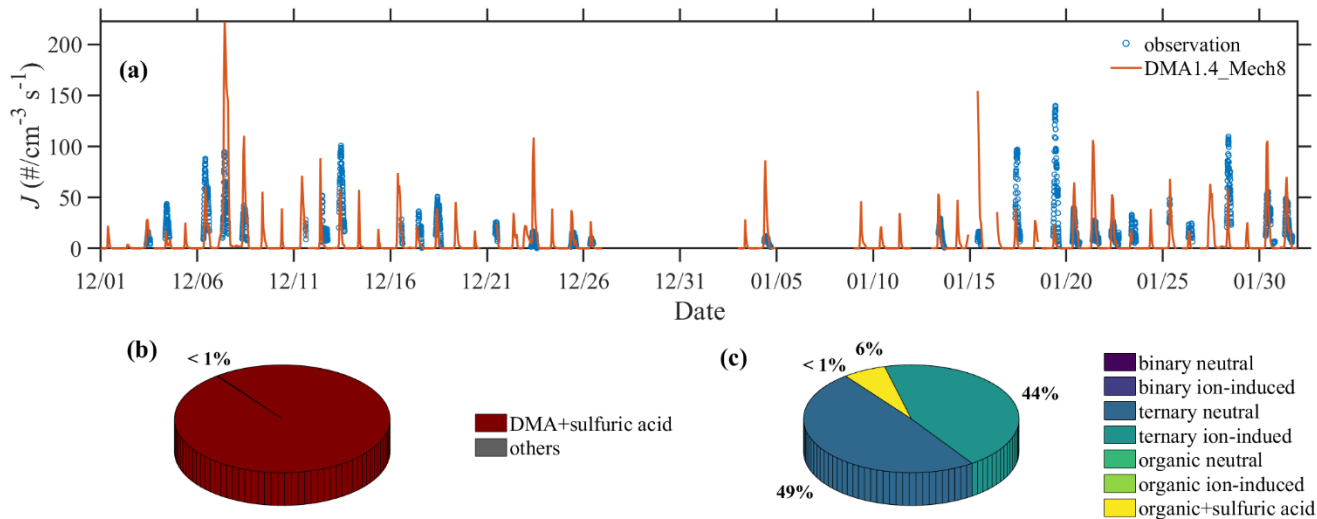
727

728 **Figure 4. Comparison of time series of particle number size distribution simulated by various scenarios with the**  
 729 **observed one.** Description of four scenarios is detailed in *Configuration of the Updated WRF-Chem/R2D-VBS Model*  
 730 section.



731

732 **Figure 5. Comparison of averaged particle number size distribution simulated by various scenarios with the observed**  
 733 **one.** Description of four scenarios is detailed in *Configuration of the Updated WRF-Chem/R2D-VBS Model* section.



734

735 **Figure 6. Comparison of simulated nucleation rates with those derived from field measurements (a), and contribution**  
 736 **from different nucleation mechanisms (b) with a special illustration of nucleation pathways other than SA-DMA (c).**